

# Quantum interference enhancement and fluorescence spectral linewidth narrowing of a four-level system via dielectric Mie resonances

Qi Liu,<sup>1,2</sup> Lingxiao Shan,<sup>1</sup> Yali Jia,<sup>1</sup> Yun Ma,<sup>1</sup> Qihuang Gong,<sup>1,2,3,4,5</sup> and Ying Gu<sup>1,2,3,4,5,\*</sup>

<sup>1</sup>State Key Laboratory for Mesoscopic Physics, Department of Physics, Peking University, Beijing 100871, China

<sup>2</sup>Frontiers Science Center for Nano-Optoelectronics and Collaborative Innovation Center of Quantum Matter and Beijing Academy of Quantum Information Sciences, Peking University, Beijing 100871, China

<sup>3</sup>Collaborative Innovation Center of Extreme Optics, Shanxi University, Taiyuan, Shanxi 030006, China

<sup>4</sup>Peking University Yangtze Delta Institute of Optoelectronics, Nantong 226010, China

<sup>5</sup>Hefei National Laboratory, Hefei 230088, China



(Received 30 September 2022; revised 14 April 2023; accepted 15 August 2023; published 5 September 2023)

Quantum interference (QI) among different spontaneous decay channels has led to many important quantum optics applications. This effect can be strongly enhanced in an anisotropic quantum vacuum (AQV) provided by photonic nanostructures, which is promising to apply in integrated photonic quantum technologies. However, the QI effect in a dielectric Mie resonance system with a large AQV has not been studied. Here, we investigate the QI enhancement and fluorescence spectral linewidth narrowing of a four-level system with a high-index dielectric nanosphere. We find that the nearly maximum QI can be obtained due to the extreme AQV under Mie resonances. We also show that the degree of QI varies in a wide range when selecting different Mie resonances and the emitter's position. We further illustrate the subnatural-linewidth narrowing of the fluorescence spectra in the Mie resonance system, which results from large QI and a relatively small Purcell factor. These findings not only provide a scheme for quantum coherence manipulation, but also have potential applications in integrated quantum photonic devices.

DOI: [10.1103/PhysRevA.108.033702](https://doi.org/10.1103/PhysRevA.108.033702)

## I. INTRODUCTION

The quantum interference (QI) effect in the spontaneous emission process can significantly change the evolution of the quantum system [1]. Based on the QI, many interesting phenomena and applications are discovered, including lasing without inversion [2–4], QI-induced absorption control [5,6], fluorescence spectra narrowing and elimination [7–13], QI-enhanced Kerr nonlinearity [14], QI-assisted quantum entanglement [15,16], and so on. Manipulating coherence between energy levels of a quantum system is a key requirement in many laser and quantum optics applications, so QI is a promising tool for future quantum technology.

To obtain a significant QI effect, transition dipole moments of two spontaneous emission channels are required to be parallel or antiparallel, which is difficult to achieve in a real experimental configuration [10,11]. In 2000, Agarwal [17] theoretically demonstrated that QI arises for a quantum system placed in an anisotropic quantum vacuum (AQV) environment, even though corresponding transition dipole moments are orthogonal. Later, it was found that nanophotonic structures can provide a large AQV [18–20] due to a highly confined anisotropic local field. To enhance the QI, various nanophotonic structures have been proposed, such as photonic crystals [21,22], metamaterials [23–31], plasmonic structures [32–37], two-dimensional materials [38–40],

topological insulator multilayers [41], and semiconductor nanocavity systems [42]. The AQV in these structures inspires people to manipulate QI phenomena at the nanoscale, including fluorescence spectra narrowing [33–35], Kerr nonlinearity enhancement [36], excited-state population trapping, and quantum entanglement [42]. Consequently, nanophotonic structures have become a favorable platform for integrated QI applications.

Although above nanostructures have many fascinating properties, the intrinsic loss of these nanostructures, which reduces the quantum yield, restricts the application of QI. Fortunately, recently developed dielectric resonant metaphotonics [43,44] can solve the problem to some extent. First, the absorption of dielectric resonance is negligible [43] in the visible and near-infrared regions. Second, high-index dielectric nanostructures support both electric and magnetic resonances [45], thus providing novel electromagnetic responses. Third, light can be trapped in a subwavelength-scale volume with low intrinsic loss [44], which can enhance the light-matter interaction [46,47]. Based on high-index dielectric nanostructures, various novel physical effects are reported, including magnetic mirrors [48], high-quality-factor supercavity modes [49,50], ideal magnetic dipole (MD) scattering [51], and the transverse Kerker effect [52–54]. Hence it offers a unique platform to realize subwavelength-scale novel electromagnetic responses. More importantly, high-index dielectric nanostructures with Mie resonances can create an extreme AQV environment [55–58], which will have great potential in QI enhancement and fluorescence manipulation.

\*ygu@pku.edu.cn

As far as we are concerned, the dielectric resonance structure is very special in the QI enhancement and its induced linewidth narrowing of fluorescence spectra. First, the anisotropy of Purcell factors is very high in dielectric resonant structures, but the Purcell factors themselves can be very small. On the one hand, this high AQV can lead to very large QI enhancement; on the other hand, small Purcell factors can guarantee that the linewidth of fluorescence spectra narrows down, sometimes even reaching subnatural linewidth. Second, the above features are obviously superior to those existing in resonant metallic nanoparticles. In metallic nanoparticles, though the QI is very high, the corresponding values of Purcell factors are also very high, which leads to very wide linewidth of fluorescence spectra [33–35]. Moreover, the absorption part of spontaneous emission is very high in metallic structures, so that only a few parts of the fluorescence can be collected, which to some extent hinders the experimental observation. Thus, the dielectric nanostructures may be a more feasible platform for studying the QI-induced spectra manipulation. However, the QI and fluorescence spectra in the dielectric resonant system have never been investigated in the visible region, where most of the atomic QI properties occur.

In this paper, we theoretically investigate the QI effect and fluorescence spectral linewidth narrowing when a four-level quantum emitter is in the vicinity of a high-index dielectric nanosphere. We find that the Mie resonances in dielectric nanostructure can greatly enhance the QI due to the extreme AQV environment. Additionally, the magnetic and electric Mie resonances can lead to QI factors with opposite signs. Furthermore, the QI factors can be modified by varying positions of the quantum emitter, and thus we can obtain the local maximum QI factor for a given Mie resonance. One interesting finding is that the minimum Purcell factor can be much less than 1 when the QI factor is large, which is different from the usual plasmon particle system. Then we further demonstrate that the linewidth of triplet fluorescence spectra can be sharply narrowed due to small Purcell factors. More specifically, the central spectral line or sidebands of the triplet can be narrowed into subnatural linewidth when the QI factor is positive or negative. Moreover, in the metallic nanoparticle, only a very small nanoscale area [33] can be used to demonstrate the phenomenon of fluorescence spectra modification because of the very wide linewidth, while in dielectric nanoparticles we will see that very high QI and a good effect on the linewidth narrowing of fluorescence spectra are available in a much larger region near the particle. These results may find potential applications in integrated quantum photonics, such as on-chip subnatural linewidth photon sources.

Note that our paper is different from Refs. [34,35,37]. In Ref. [37], although QI enhancement is also obtained in the high-permittivity dielectric system for terahertz waves, the system is a thick slab where Mie resonances are absent. A sphere geometry is also studied in Ref. [37] as well as in Refs. [34,35], but the high-permittivity material is plasmoniclike with  $\text{Re}(\varepsilon) < 0$ , while in our system the high-permittivity material has a dielectric response with  $\text{Re}(\varepsilon) > 0$  which yields multipole Mie resonances.

The paper is organized as follows. In Sec. II, we set up the physical model and present the basic equations to analyze the QI effect as well as spontaneous emission spectra. The

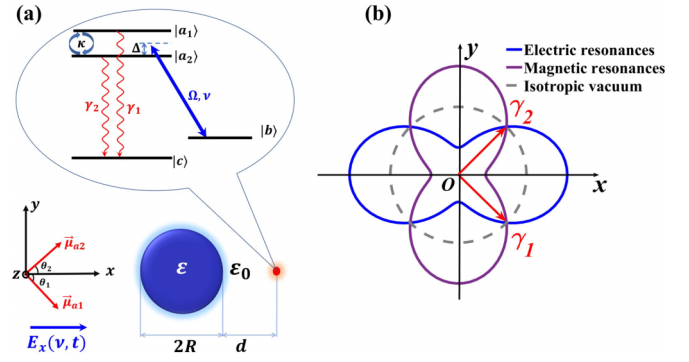


FIG. 1. (a) The schematic of the composite system with dielectric sphere and four-level quantum emitter. A dielectric sphere with relative permittivity  $\varepsilon$  and radius  $R$  is placed in the medium with relative permittivity  $\varepsilon_0$ . A quantum emitter is in the vicinity of the sphere surface with a distance  $d$  either inside or outside the sphere. The transition dipole moments of two close-lying upper levels are linearly polarized and orthogonal to each other in the  $xy$  plane. (b) A sketch of anisotropic quantum vacuum induced by Mie resonances. Two polar curves correspond to anisotropic spontaneous emission rates induced by electric (blue curve, concave along  $y$  axis) and magnetic resonances (purple curve, concave along  $x$  axis), resulting in the nonzero cross-damping rate ( $\kappa \neq 0$ ) between two upper levels.

QI enhancement by Mie resonances is discussed in Sec. III. Then fluorescence spectrum manipulation is demonstrated in Sec. IV. We also give a brief discussion about the influence of phase factors on our results in Sec. V. Finally, we conclude in Sec. VI.

## II. MODEL SETUP

Consider a four-level quantum emitter in the vicinity of a high-index dielectric sphere, as shown in Fig. 1(a). The nonabsorbing dielectric sphere with radius  $R$  and relative permittivity  $\varepsilon$  is centered at the coordinate origin, surrounded by air with relative permittivity  $\varepsilon_0 = 1$ . For simplification, the dielectric is assumed to be a perfect continuous medium without dispersion and loss. The quantum emitter with a distance  $d$  away from the spherical surface is situated outside or inside the sphere. The quantum emitter has two close-lying upper levels  $|a_1\rangle$  and  $|a_2\rangle$  and two ground states  $|b\rangle$  and  $|c\rangle$  with the energies  $\hbar\omega_{a_1}$ ,  $\hbar\omega_{a_2}$ ,  $\hbar\omega_b$ , and  $\hbar\omega_c$ . A coherent field with frequency  $\nu$  drives transitions  $|a_1\rangle \leftrightarrow |b\rangle$  and  $|a_2\rangle \leftrightarrow |b\rangle$  with the same Rabi frequency intensity  $|\Omega|$ , while the phase difference between two Rabi frequencies is  $\phi$ . The detunings are  $\Delta = \nu - (\omega_{a_2} - \omega_b)$  and  $\Delta' = \nu - (\omega_{a_1} - \omega_b) = \Delta - \omega_{12}$ , where  $\omega_{12} = \omega_{a_1} - \omega_{a_2}$ . Here, the four-level system is driven by the local field whose central frequency is locked at the transition frequency. The local field is a sum of the external plane wave and the scattered field, i.e.,  $\mathbf{E}(\mathbf{r}_0) = \mathbf{E}_{\text{in}}(\mathbf{r}_0) + \mathbf{E}_{\text{sca}}(\mathbf{r}_0)$ , while  $\mathbf{r}_0 = (R + d, 0, 0)$  is the coordinate of the emitter's position. The external plane wave propagates along the positive  $z$  axis with the electric field polarized along the  $x$  axis,  $\mathbf{E}_{\text{in}}(\mathbf{r}_0) = E_0 \mathbf{e}_x e^{ik_0 \mathbf{r}_0 \cdot \mathbf{e}_z}$ , while the scattered field  $\mathbf{E}_{\text{sca}}(\mathbf{r}_0)$  can be obtained based on the Mie theory [59] or full-wave simulation. With a proper plane-wave intensity, the local field can yield a Rabi frequency  $|\Omega| = 5\gamma_0$  ( $\gamma_0$  is the emission rate of the emitter in vacuum). We give a quantitative estimation about

the income field intensity. With a dielectric sphere of radius  $R = 220$  nm and permittivity  $\varepsilon = 10$ , the near-field enhancement is about  $f = |\mathbf{E}_{\text{sca}} + \mathbf{E}_{\text{in}}|/|\mathbf{E}_{\text{in}}| \approx 1-10$  according to the Mie theory [59]. To yield a Rabi frequency  $|\Omega| = 5\gamma_0$ , the incident field amplitude is  $|\mathbf{E}_{\text{in}}| = 5\hbar\gamma_0/f\mu_0$ , where  $\mu_0$  is the transition dipole moment. Then, the intensity of the incident light approximates to  $I_{\text{in}} = c\varepsilon_0|\mathbf{E}_{\text{in}}|^2 = 25c\varepsilon_0\hbar^2\gamma_0^2/f^2\mu_0^2$ . For reference, we assume  $\gamma_0 = 1 \text{ ns}^{-1}$  and  $\mu_0 = 1 \text{ eÅ}$ , and then the field intensity  $I_{\text{in}} \approx 0.029-2.9 \times 10^5 \text{ mW/cm}^2$ . If the incident light is a Gaussian beam with beam waist radius  $r = 100 \mu\text{m}$ , then the power of the pump field  $P_{\text{in}} = I_{\text{in}}\pi r^2 \approx 0.9-90 \text{ mW}$ .

Under electric dipole (ED) and rotating-wave approximations, the Hamiltonian in the interaction picture is written as [33]

$$H_I = -\hbar(\Delta'|a_1\rangle\langle a_1| + \Delta|a_2\rangle\langle a_2|) + \hbar\Omega(|a_1\rangle\langle b| + e^{i\phi}|a_2\rangle\langle b| + \text{H.c.}). \quad (1)$$

Applying Weisskopf-Wigner approximation and tracing out the photon bath, we obtain the quantum master equation [42]

$$\dot{\rho} = -\frac{i}{\hbar}[H_I, \rho] + \sum_{j,k=a_1,a_2} \Gamma_{j,k} \left( \sigma_{c,j} \rho \sigma_{k,c} - \frac{1}{2} \{ \sigma_{j,c} \sigma_{c,k}, \rho \} \right). \quad (2)$$

Here,  $\sigma_{\alpha,\beta} = |\alpha\rangle\langle\beta|$  ( $\alpha, \beta = a_1, a_2, b, c$ ) is transition dipole operator between energy levels  $|\alpha\rangle$  and  $|\beta\rangle$ .  $\Gamma_{a_1,a_1} = \gamma_1$  ( $\Gamma_{a_2,a_2} = \gamma_2$ ), which comes from the interaction with a photonic reservoir of Mie resonances, is the spontaneous emission rate between levels  $|a_1\rangle$  ( $|a_2\rangle$ ) and  $|c\rangle$ .  $\Gamma_{a_1,a_2} = \Gamma_{a_2,a_1}^* = \kappa$  is the cross-damping rate between two upper levels, originating from the interaction with the common vacuum provided by Mie resonances.

Mie resonances of the dielectric sphere can create an AQV environment. For a dipole moment  $\vec{\mu}(\theta) = |\vec{\mu}|(\cos\theta\mathbf{e}_x + \sin\theta\mathbf{e}_y)$  whose orientation angle to the  $x$  axis is  $\theta$ , its spontaneous emission rate is given by  $\gamma(\theta) = \gamma_{xx}\cos^2\theta + \gamma_{yy}\sin^2\theta$  [17,20]. Here, we assume that the quantum axis of the emitter is along the  $z$  axis and that  $\gamma_{xx}$  and  $\gamma_{yy}$  are emission rates for the dipole moment along  $x$  and  $y$  axes, which are also maximum or minimum emission rates in the  $xy$  plane for the given position. In an isotropic quantum vacuum,  $\gamma_{xx} = \gamma_{yy}$  [gray dashed curve in Fig. 1(b)]. However, for the AQV,  $\gamma_{xx} \neq \gamma_{yy}$ . Figure 1(b) sketches the emission rates for AQV created by electric resonances (blue curve, concave along the  $y$  axis) and magnetic resonances (purple curve, concave along the  $x$  axis). The values of  $\gamma_{xx}$  and  $\gamma_{yy}$  of different types of Mie resonances will be discussed in the next section.

The AQV can induce QI, whose degree can be characterized by the cross-damping rate in Eq. (2). The cross-damping rate between two upper levels is given by  $\kappa_{12} = (2\omega^2/\hbar\varepsilon_0c^2)\vec{\mu}_{a_1}^* \cdot \text{Im}\{\vec{\mathbf{G}}(\mathbf{r}_0, \mathbf{r}_0; \omega)\} \cdot \vec{\mu}_{a_2}$  [17], where  $\text{Im}\{\vec{\mathbf{G}}(\mathbf{r}_0, \mathbf{r}_0; \omega)\} = C_{xx}\mathbf{e}_x\mathbf{e}_x + C_{yy}\mathbf{e}_y\mathbf{e}_y + C_{zz}\mathbf{e}_z\mathbf{e}_z$  is the imaginary part of the anisotropic dyadic Green's function. Here,  $\mathbf{r}_0 = (R+d)\mathbf{e}_x$  is the position of the emitter, and  $C_{yy} = C_{zz} \neq C_{xx}$  is satisfied due to the spherical symmetry. The existence of QI is indicated by a nonzero value of  $\kappa$ . Obviously,  $\kappa$  is strongly dependent on the relative phase factor between two dipoles as well as their orientations in the given posi-

tion. The former may cause  $\kappa$  to become a complex number, where the latter will change the amplitude  $|\kappa|$ . For example, if two orthogonal dipoles orient as  $\vec{\mu}_{a_1} = \mu_0(\mathbf{e}_x + i\mathbf{e}_y)/\sqrt{2}$  and  $\vec{\mu}_{a_2} = \mu_0\mathbf{e}_z$ , then  $\kappa = 0$ , which means no QI exists for such a choice of dipole orientations. For simplification, we only consider orthogonal dipoles oriented in the  $xy$  plane. To obtain the optimal  $|\kappa|$ , one can choose two linearly polarized dipoles  $\vec{\mu}_{a_1,a_2} = \mu_0(\mathbf{e}_x \pm \mathbf{e}_y)/\sqrt{2}$  [33] or circular polarized dipoles  $\vec{\mu}_{a_1,a_2} = \mu_0(\mathbf{e}_x \pm i\mathbf{e}_y)/\sqrt{2}$  [32]. As pointed out in Ref. [25], the choices of two linear or circular orthogonal dipoles are equivalent (assuming anisotropic axes are  $x$  and  $y$  axes), which leads to the same emission rates and cross-damping rate. Both choices can be achieved in a real quantum emitter system; for example, circular dipoles are common in atom systems [17], while linear dipoles can be found in quantum dot systems [42]. In this paper, we choose two linearly polarized dipoles as shown in Fig. 1. But results should not change for two circularly polarized dipoles. Here,  $|\vec{\mu}_{a_1}| = |\vec{\mu}_{a_2}|$ . In this case, spontaneous emission rates of two decay channels are  $\gamma_1 = \gamma_2 = (\gamma_{xx} + \gamma_{yy})/2$  and cross damping is  $\kappa = (\gamma_{xx} - \gamma_{yy})\exp(i\Delta\varphi)/2$ , where  $\Delta\varphi$  is the relative phase difference between two orthogonal dipoles. We can use the Purcell factor to describe the emission enhancement by  $F_{x,y} = \gamma_{xx,yy}/\gamma_0$  [19], where  $\gamma_0$  is the spontaneous emission rate in a free vacuum. Then, we define the effective QI factor as

$$I_q = \text{Re}\left(\frac{\kappa}{\sqrt{\gamma_1\gamma_2}}\right) = \frac{F_x - F_y}{F_x + F_y} \cos(\Delta\varphi). \quad (3)$$

The definition of the QI factor is consistent with previous work [23] when  $\Delta\varphi = 0$ . We will see later that one should keep two dipoles in phase ( $\Delta\varphi = 0$ ) or out of phase ( $\Delta\varphi = \pi$ ) to obtain an obvious modification effect. When  $\Delta\varphi = 0$ , the QI factor is only determined by the AQV environment, i.e., the larger difference between  $F_x$  and  $F_y$  will lead to a stronger interference effect. In the following, we will see that the sign of  $F_x - F_y$  is opposite for high-order electric and magnetic Mie resonances, which leads to different interference features. Here, we ignore the local-field corrections of Purcell factors, which should be considered when the emitter is embedded in a real dielectric medium (not perfectly continuous) [60,61]. This is reasonable in our analysis of QI, because both  $F_x$  and  $F_y$  feel the same corrections when the permittivity is very large, so QI will not change even if we consider the local-field corrections. In addition, the corrections to the Purcell factor will broaden the linewidth of emission spectra, which is not discussed here.

The QI effect has an obvious impact on the fluorescence spectra. The spectra can be obtained from  $S(\omega) = \lim_{t \rightarrow \infty} \text{Re}[ \int_0^{+\infty} d\tau \sum_{k=a_1,a_2} \langle \sigma_{k,c}(t) \sigma_{c,k}(t+\tau) \rangle e^{i(\omega-\nu_0)\tau} ]$  [62], where  $\nu_0$  is the frequency from the middle of the two upper levels to the level  $|c\rangle$ . Under dressed state analysis, we know that the spectra are triplets [33], including one central peak at  $\omega_0 = \nu_0$  and two side peaks at  $\omega_{\pm} = \nu_0 \pm \sqrt{8\Omega^2 + \omega_{12}^2}/2$ . What is more, when two upper levels are nearly degenerate such that  $\omega_{12}^2 \ll 8\Omega^2$ , the spectral linewidths of the three peaks can be expressed as  $\Gamma_0 = \gamma(1 - I_q)$  and  $\Gamma_{\pm} = \frac{\gamma}{2}(1 + I_q)$  [33], where  $\gamma = \gamma_1 = \gamma_2$  is the central peak spectral linewidth when the quantum interference effect is absent ( $I_q = 0$ ). We can see that

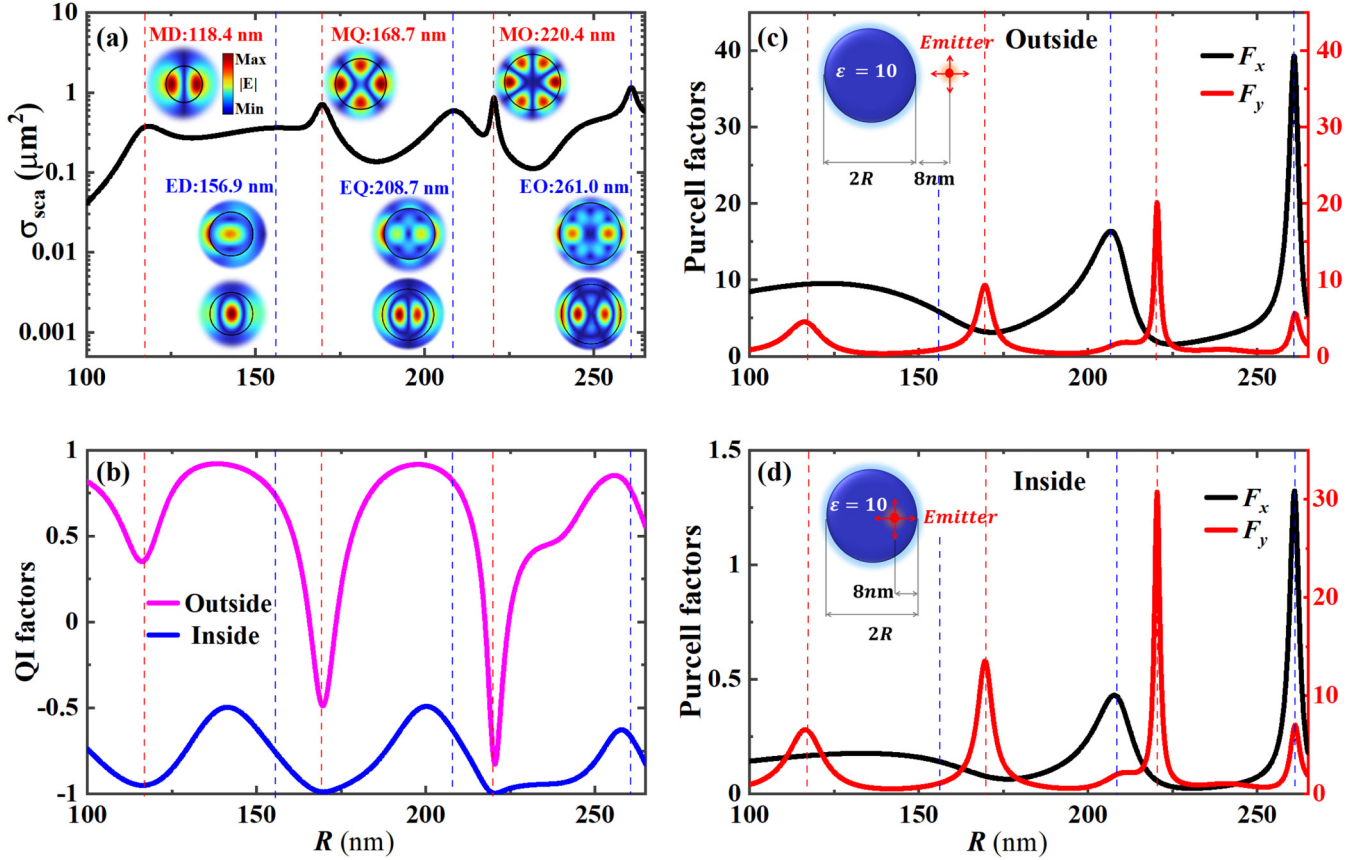


FIG. 2. Enhanced QI effect with varying sphere radius  $R$ . (a) Scattering cross section  $\sigma_{\text{sca}}$  as a function of radius  $R$  for an incident plane wave. The insets show the near-field patterns of the first six Mie resonances; the dashed lines and the texts indicate the  $R$  parameters for each resonance. (b) QI factor for varying radius  $R$ . The pink (upper) curve denotes the quantum emitter outside the sphere, while the blue (lower) curve denotes the emitter inside the sphere. Anisotropic Purcell factors of an emitter (c) outside and (d) inside the sphere are presented. The black (three-peaked) and red (five-peaked) curves correspond to the Purcell factors of  $x$ - and  $y$ -polarized transition dipole moments. Insets illustrate the system setup for emitter outside and inside cases. In all figures, the permittivity of the sphere is  $\epsilon = 10$ , and the excitation wavelength is at  $\lambda_0 = 780$  nm.

QI strongly modifies the linewidths of spectra. For  $I_q > 0$ , the central peak is narrowed and the side peaks are broadened; for  $I_q < 0$ , the central peak is broadened and the side peaks are narrowed. According to Eq. (3), two orthogonal dipoles should be in phase or out of phase to keep a large QI factor, which helps to obtain obvious linewidth modification. For simplification, we assume  $\Delta\varphi = 0$  in our later discussion. In our numerical calculation, small incoherent pumps from ground state  $|c\rangle$  to excited states  $|a_1\rangle$  and  $|a_2\rangle$  are applied to obtain steady-state fluorescence spectra [9]. The small incoherent pumps will result in slight differences between theoretical prediction and numerical calculation of the spectral linewidths. We will see later that Mie resonances can provide rich modification for fluorescence spectra through QI.

The calculation methods used in this paper are described as follows. The Mie resonances are obtained from the scattering cross section  $\sigma_{\text{sca}}$  (see Appendix A). Then, the anisotropic Purcell factor  $F_{x,y}$  (see Appendix B) is calculated using the expressions obtained in Ref. [63]. We also perform electromagnetic simulations using finite element methods (commercial COMSOL software) to visualize the near-field patterns of Mie resonances. The simulation results also agree

with those obtained from formulas in Appendices A and B. The master equation (2) and fluorescence spectra  $S(\omega)$  are solved numerically using the quantum toolbox in PYTHON (QUTIP) [64].

### III. QUANTUM INTERFERENCES ENHANCED BY MIE RESONANCES

The nanostructures with high permittivity support two types of Mie resonances, i.e., electric-type and magnetic-type [43,44] resonances. Their distinct anisotropic near-field distributions lead to anisotropic Purcell factors, and so to AQV, which will have an enhancement effect on QI. In this section, QI enhancement under Mie resonances is investigated with varying dielectric sphere radius  $R$ . Then, the influences of permittivity  $\epsilon$  and emitter position on QI are discussed.

#### A. The effect of Mie resonances with different radii $R$

We first consider Mie resonances of the dielectric sphere with different radii. Figure 2(a) shows scattering cross section  $\sigma_{\text{sca}}$  as a function of sphere radius  $R$ . Here the sphere permittivity is  $\epsilon = 10$ , and the excitation wavelength is at

$\lambda_0 = 780$  nm. According to the Mie theory [59], as  $R$  increases from 100 to 260 nm, six resonant peaks appear successively, corresponding to MD, ED, magnetic quadrupole (MQ), electric quadrupole (EQ), magnetic octupole (MO), and electric octupole (EO) resonances, respectively. Magnetic-type resonances result from the circular displacement currents supported by the dielectric medium [43], which are lacking in plasmonic particles. Here, two kinds of electric-type resonances, with angular mode indices  $m = 0$  and  $|m| = 1$ , are available when excited by the  $x$ - and  $y$ -polarized dipole, respectively. The local fields of these two kinds of modes are shown in the second-row (for  $m = 0$ ) and the third-row (for  $|m| = 1$ ) insets of Fig. 2(a), while the first-row insets show the local fields of magnetic resonances (with  $|m| = 1$ ). We see that the local fields are more concentrated inside the high-index dielectric sphere for resonances with mode indices  $|m| = 1$ , while for resonances with mode indices  $|m| = 0$  the local fields are more confined at the outer boundary of the sphere. These differences in near-field distributions lead to distinct AQV features for two types of resonances.

Then, the anisotropic Purcell factors induced by Mie resonances are investigated, which are the origin of AQVs. Figures 2(c) and 2(d) show anisotropic Purcell factors as sphere radius  $R$  changes when the emitter is outside and inside the sphere, respectively. Here, the distance is  $d = 8$  nm. We can observe that the Purcell factors of the  $y$ -polarized dipole ( $F_y$ ) have a factor of 5 enhancement approximately near the MD resonance, and then the enhancements become larger for the higher-order magnetic resonances. A smaller enhancement of  $F_y$  also arises near the electric-type resonances. As for Purcell factors of the  $x$ -polarized dipole ( $F_x$ ), the significant enhancements only appear near the electric-type resonance. Although both  $F_x$  and  $F_y$  are enhanced near the electric-type resonances, the former is mainly contributed by resonances with mode indices  $m = 0$  while the latter is mainly provided by resonances with mode indices  $m = 1$  [63]. With the given conditions in Figs. 2(c) and 2(d), the Purcell enhancements of  $F_x$  and  $F_y$  for the dipole inside the sphere [Fig. 2(c)] are weaker (for  $F_x$ ) or stronger (for  $F_y$ ) than values for the dipole outside the sphere [Fig. 2(d)]. This is because Purcell factors become larger in the region with a stronger near-field intensity [19]. For both electric and magnetic resonances, the enhanced Purcell factors are much smaller than those obtained in plasmonic structures, where the large Purcell enhancement is due to the large near-field enhancement originating from collective oscillations of free electrons [18,19,65]. But the nonradiative part of the Purcell factor in plasmonic structures is also large because of large intrinsic loss [19]. Hence Mie resonances in the dielectric sphere lead to a large difference between  $F_x$  and  $F_y$ , and thus high AQVs are created.

Next, we discuss the QI enhancement induced by AQVs under Mie resonances. Figure 2(b) shows variations of QI factors as an increment of  $R$ . The pink (upper) and blue (lower) curves show the cases in which the emitter is outside and inside the sphere. In most cases, the absolute values of QI factors for Mie resonances (marked by dashed lines) are greater than 0.5, except that  $I_q \approx 0.35$  for MD. This enhancement is a result of large AQVs under Mie resonances. The QI factor can be further modulated via rich variation of AQVs among different Mie resonances. What is more, the QI factor can even

approach  $\pm 1$  (the theoretical boundary for maximum QI) by placing the emitter inside the sphere [blue (lower) curve in Fig. 2(b)] when magnetic resonances happen. Such a large QI factor comes from extreme AQV, where Purcell factor  $F_y$  is enhanced and  $F_x$  is suppressed, as shown in Fig. 2(d). Similar to many nanostructures proposed in the literature [22,32,37–39,41], a large QI factor is obtained when the emitter is close to the structure interface ( $d/\lambda_0 \ll 1$ ) because extreme AQV is only available in the near-field region. Note that for the case of the quantum emitter inside the sphere the large QI factors are associated with a small Purcell factor in a large parameter region [the first four Mie resonances in Fig. 2(d)]. It is different from the case in metallic nanoparticles, where the large QI factor ( $|I_q| \approx 1$ ) is accompanied by a large Purcell factor [33]. This feature indicates that the dielectric Mie resonance system is an ideal system to demonstrate the QI effect in fluorescence spectra.

Furthermore, the sign of the QI factor can be modified by different types of Mie resonances. As shown in Fig. 2(b), for the emitter outside the sphere (upper pink curve), the QI factor is positive in electric resonances, while it becomes negative in higher-order magnetic resonances. The reason is polarization-dependent Purcell enhancement, i.e., that  $F_x$  is dominant for electric resonances while  $F_y$  is dominant for magnetic resonances (except for MD resonances), and the sign of  $F_x - F_y$  is the same as that of the QI factor according to the definition in Eq. (3). Based on this, the QI factor can be changed almost from  $-1$  to  $+1$ . Although the sign of the QI factor can also be altered in other structures, the variation range of QI factor is smaller than our result because these structures only support one type of electromagnetic response [21,23,37–39,41].

Another interesting result is that the QI enhancement is also available in some electric resonance-detuned structures. For the emitter outside the sphere, the local maxima of QI factors are obtained under detuned conditions with a small geometrical departure from electric resonant structures [upper pink curve in Fig. 2(b)], although QI factors for exact electric resonances are also large. This can be understood as follows. When the emitter is outside the sphere, the Purcell enhancement of the  $x$ -polarized dipole is mainly provided by electric-type resonance, while the Purcell enhancement for the  $y$ -polarized one is mainly contributed by magnetic-type resonances. Note that the linewidths of electric resonances are relatively broad, so a relatively large Purcell factor  $F_x$  is still available when the structure slightly departs from the electric resonant one [Fig. 2(c)]. However, the structure is now far off resonant from magnetic resonances, and thus the Purcell factor of the  $y$ -polarized dipole ( $F_y$ ) will be largely suppressed [Fig. 2(c)]. As a result, the AQV becomes stronger when the excitation wavelength is slightly detuned from electric resonances, which leads to a larger QI factor. A more detailed discussion is available in Appendix C. For the emitter inside the sphere, the resonance-detuned structures can also lead to a large QI factor with  $|I_q| > 0.5$  [lower blue curve in Fig. 2(b)]. In this case, it is also caused by different suppressed ( $F_x$ ) or enhanced ( $F_y$ ) degrees of Purcell factors. Different from these works of QI enhancement relying on structure resonance [21,32,33], a resonance-detuned dielectric sphere can lead to both Purcell factors less than 1 while  $|I_q|$  can still approach 0.5, which is hopeful for effectively narrowing the spectral

linewidth. The QI experiments may also benefit from the detuning QI enhancement because it can reduce the strict requirement for accurate sample preparation.

### B. The influences of permittivity $\varepsilon$ and emitter position on QI

Let us now briefly discuss the influences of permittivity  $\varepsilon$  and emitter position on QI. First, we discuss the impact of permittivity. Mie resonances are sensitive to the changes of  $\varepsilon$ . A higher permittivity leads to much tighter field confinement. So, a more considerable enhancement of Purcell factors is produced under resonant conditions, while the Purcell suppression becomes more pronounced under off-resonant conditions. As a result, the AQV becomes stronger in the higher permittivity structure, leading to a stronger QI enhancement to some extent. The high permittivity of the sphere ensures that Mie resonances can be obtained with a very small radius. For a realistic dielectric material, however, the permittivity cannot be as high as one wishes so the radius cannot be arbitrarily small. In the visible region, a high permittivity of  $\approx 10$  is accessible [66], which guarantees that Mie resonances and induced large QI can still be realized in the sphere with a larger radius of  $\approx \lambda/2\sqrt{\varepsilon}$  [43,59]. A more detailed discussion on Mie resonances with a larger radius and relatively smaller  $\varepsilon$  is available in Appendix D. Thus, generating a strong QI enhancement is easier with a higher-permittivity sphere.

Then, we discuss the influence of the emitter's position. Given a specific dielectric sphere structure under magnetic (electric) resonance, the spatial profile of Purcell factor  $F_y$  ( $F_x$ ) is similar to the corresponding near-field distribution. Accordingly, a large AQV arises near the hot spot regions of the resonant near field. Therefore, large QI is accessible near the inner or outer surface of the sphere for magnetic or electric resonances. In addition, a relatively large QI arises between the center and surface of the sphere. Moreover, a spatial region with a width of  $\approx 100$  nm can provide a large QI factor ( $|I_q| > 0.5$ ) while also maintaining relatively low Purcell factors. Such a region is several times broader than that in plasmonic structures [33–35]. A more detailed discussion on the emitter's position is available in Appendix E. Hence, the QI factor can be adjusted flexibly by selecting the emitter's position.

As can be seen from the above discussions, QI enhancement is highly alterable in Mie resonant sphere structures. We can not only optimize the parameters to achieve a large QI and small Purcell factors, but also modulate the sign of the QI factor. These features can be used to manipulate the fluorescence spectra more flexibly.

## IV. FLUORESCENCE SPECTRUM CONTROL VIA MIE RESONANCES

In previous sections, we show that the Mie resonance in the high-index dielectric sphere can provide a large AQV to enhance QI. At the same time, we notice that Purcell factors are restricted to a relatively small value for low-order Mie resonances. Even though one of the Purcell factors ( $F_x$ ,  $F_y$ ) may be largely enhanced for some parameters, it is still possible to keep the other factor small, which is very different from the AQV feature of plasmon structure that usually dramatically

enhances both factors [32,33]. In a realistic quantum optics experiment, the detuning between the driving field and energy levels needs to be considered. Thus, the driving Rabi frequency should be limited to  $\Omega < 10\gamma_0$  to avoid saturation. If the radiation rate is too large, then the linewidth of the fluorescence spectrum is too broad to observe an obvious QI effect. For Mie resonances we investigate here, the radiation rate of the emitter can be less than  $14\gamma_0$ . Hence the spectral peaks will be well separated, which also provides us a powerful method to control fluorescence spectra. However, the region where large QI factors and small Purcell factors are coincident in metallic nanoparticle systems only covers several tens of nanometers in the visible region [32,33], much smaller than we obtained in the Mie resonances system ( $\Delta x \approx 100$  nm). Also, the collection of fluorescence will be more efficient in the dielectric system than in plasmon structures, because the absorption part of spontaneous emission is very high in the latter case. So, dielectric Mie resonant structures may be more feasible to demonstrate the QI effect in fluorescence spectra.

The fluorescence spectra  $S(\omega)$  are numerically calculated following the method in Sec. II. The center wavelength of transition between the upper levels ( $|a_1, a_2\rangle$ ) and lower level ( $|c\rangle$ ) is near  $\lambda_0 = 780$  nm, corresponding to Mie resonances wavelength; two upper levels are closely lying. Such a four-level quantum emitter may be found in rare-earth ions [67], color centers [68], or quantum dots [69], which may be integrated into the dielectric nanosphere. The driving Rabi frequency is fixed to  $\Omega = 5\gamma_0$ , and it drives the transitions on resonance and thus  $\Delta = \nu - (\omega_{a_2} - \omega_b) = 0$ , where  $\nu$  is the center frequency of the driving field. Here, we use the Mie resonances obtained in Fig. 2 with dielectric permittivity  $\varepsilon = 10$ . Note that the relative phase  $\phi$  between two Rabi frequencies can also modify the fluorescence spectra [12], which is a field-induced coherence effect. To distinguish such an effect with Mie-resonance-induced QI, we first set  $\phi = 0$  to investigate the fluorescence spectra modification so that only QI works. Then we will give a brief discussion about the additional modification provided by the phase difference  $\phi$ .

We first demonstrate the modification of fluorescence spectra  $S(\omega)$  for the emitter inside the sphere with distance  $d = 8$  nm, as illustrated in Fig. 3(a). Figures 3(b) and 3(c) show the fluorescence spectra of the first three magnetic and electric Mie resonances. As a reference, the spectra with a typical triplet in the vacuum are shown with short-dotted green curves. For the magnetic resonances [Fig. 3(b)], the spectra only have two ultranarrow sidebands, while the central peak is too broad to be observed. For the electric resonances [Fig. 3(c)], we can first observe a triplet with two narrow sidebands when ED resonance happens (lowest black curve); the central peak linewidth of the triplet is narrower than the one of the spectra in vacuum as well. As the resonances turn to EQ and EO, the linewidths of the triplet gradually become broader (the central peak of EQ and all peaks of EO) than those in the vacuum. The spectral narrowing or broadening results from the anisotropic Purcell factor as well as the QI factor. More precisely, from the dressed state analysis [33], the central linewidth is approximately given by  $\Gamma_0/\gamma_0 = (F_x + F_y)(1 - I_q)/2$ , while the sideband linewidth is given by  $\Gamma_{\pm}/\gamma_0 = (F_x + F_y)(1 + I_q)/4$ . For the emitter

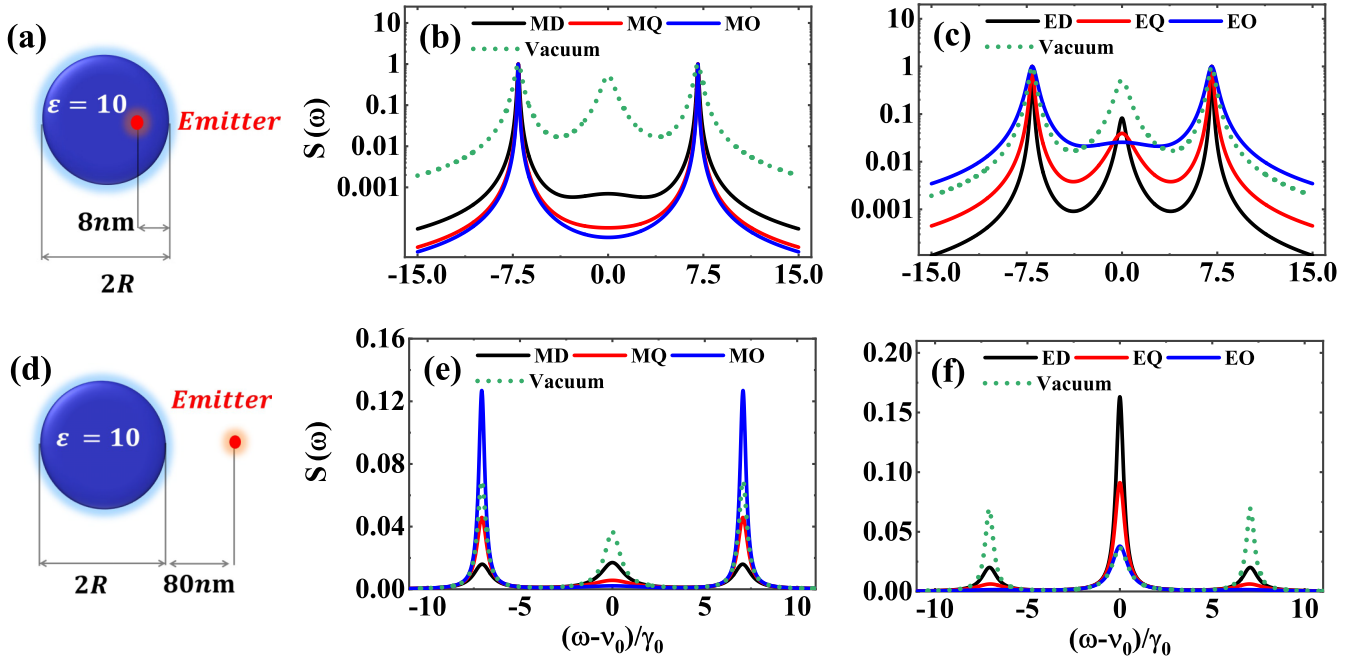


FIG. 3. Fluorescence spectra modification via different Mie resonances. (a) System setup with a quantum emitter inside the sphere. (b, c) Fluorescence spectra  $S(\omega)$  of the first three (b) magnetic resonances and (c) electric resonances for the setup (a). (d) System setup with a quantum emitter outside the sphere. (e, f) Fluorescence spectra  $S(\omega)$  of the first three (e) magnetic and (f) electric resonances for the setup (d). Here,  $\nu_0$  is the central frequency of the fluorescence emission when the driving field is absent; the system parameters are  $\Omega = 5\gamma_0$ ,  $\omega_{12} = 0$ ,  $\Delta = 0$ ; while the radius for each resonance is the same as that in Fig. 2.

located inside the sphere, as discussed in Sec. III A, all the Mie resonances induce a negative QI factor with magnitudes  $|I_q| > 0.5$ , and thus the sidebands tend to be narrowed while the central peak is broadened. Especially, the QI factors at the magnetic resonance are almost equal to  $-1$  so that the sidebands can be narrowed into the subnatural linewidth. But for the EO resonance the summation of the anisotropic Purcell factor  $F_x + F_y$  is large, which leads to the broader sideband linewidth. Hence, Mie resonances can greatly broaden the central peak and sharply narrow the sidebands of the triplet spectrum when the emitter is inside the sphere.

Then, the modification of fluorescence spectra for the emitter outside the sphere is discussed, as illustrated in Fig. 3(d). Figures 3(e) and 3(f) show the fluorescence spectra  $S(\omega)$  of the first three magnetic and electric Mie resonances. Unlike the case inside the sphere, the distance between the emitter and the sphere surface is fixed at  $d = 80$  nm rather than 8 nm to obtain a suitable (relatively small) spontaneous emission rate. Otherwise, the linewidths of the spectra will be too broad to observe the QI as we discussed at the beginning of this section. First, the MD resonance leads to a broadening of all three peaks of the triplet [black curve in Fig. 3(e), whose side peak value is smallest] compared with the spectra obtained in vacuum, which is a result of a small positive QI factor and the slight Purcell enhancement. As the mode changes to the higher-order magnetic resonance such as MQ or MO, the sidebands become narrower and the central peak becomes broader due to a large magnitude QI factor but with a negative value. For the electric resonances, the center peak of the triplet spectra is narrowed while the sidebands are broadened [Fig. 3(f)]. We can also see that the higher-order electric resonances lead

to less narrowing of the central peak and a larger broadening of sidebands. This is because the first three electric resonances provide a positive QI factor around 0.6, but the Purcell factors are larger for higher-order resonances. Hence, Mie resonances can either broaden or narrow the triplets when the emitter is outside the sphere.

The above results only show the modification of fluorescence spectra when the emitter is close to the inner or outer surface of the sphere. As discussed in Sec. III B, the QI changes significantly when the emitter moves inside the sphere, which can bring large modifications to the fluorescence spectra. So, we further explore the modification of fluorescence spectra when changing the emitter's position inside the sphere. As an example, we first consider the case that the emitter is inside the sphere for the MQ resonance, as indicated in Fig. 4(a), with the emitter's position is at  $d/R = 0.05, 0.15, 0.30$ . Figure 4(b) shows the spectra of the emitter at different positions for the MQ resonance. Due to the existence of the negative QI factor, the sidebands are very narrow while the central peak is too broad to be observable. As the emitter's position changes from  $d/R = 0.05$  to 0.3, both sidebands and the central peak become broader because of the smaller magnitude of the QI factor and larger Purcell factors. Then we consider the case for the EQ resonance, as indicated in Fig. 4(c). Figure 4(d) shows the corresponding spectra of the emitter at different positions. The sidebands are a little narrower than the vacuum spectrum, but the central peak is much broadened for  $d/R = 0.05$ , which comes from the negative QI factor. When the emitter's position changes to  $d/R = 0.3$ , the central peak becomes narrower than the vacuum spectrum, while the sidebands are much broadened.

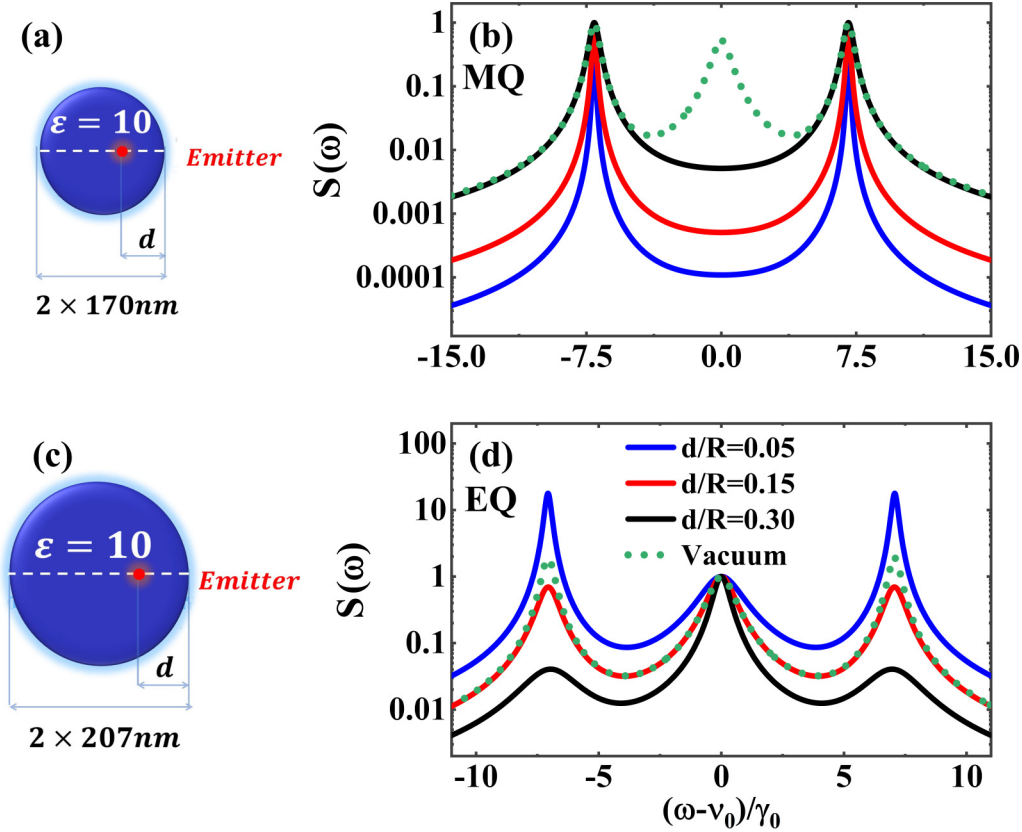


FIG. 4. Fluorescence spectra  $S(\omega)$  modification via varying the quantum emitter's position. (a, c) System setups for (a) magnetic quadrupole and (c) electric quadrupole resonances. Spectra  $S(\omega)$  for the quantum emitter placed in  $d/R = 0.05$  [blue curve, the lower one in (b) and the upper one in (d)],  $d/R = 0.15$  [red (middle) curve], and  $d/R = 0.3$  [black curve, the upper one in (b) and the lower in (d)] are shown in (b) for magnetic quadrupole and (d) for electric quadrupole resonances. All spectra are calculated under  $\Omega = 5\gamma_0$ ,  $\omega_{12} = 0$ ,  $\Delta = 0$ .

The transition of the spectra comes from the fact that the QI factor changes from negative to positive as the emitter is closer to the sphere center. In most previous studies, large QI ( $|I_q| > 0.5$ ) is either positive or negative under various QI enhancement mechanisms [23,27,28,32,37]. For these schemes, it is difficult to observe the linewidth narrowing for both the center line and sidebands in the same structures. But such manipulation is much easier to obtain in dielectric resonant structures. Therefore, the variation of the emitter's position can also bring a flexible modification to the triplet.

## V. THE INFLUENCE OF PHASE FACTORS ON EMISSION SPECTRA AND QI FACTOR

In the formal section, we concentrate on the impact of Mie resonances on QI and the modifications they bring about in the fluorescence spectra. So, the relative phase ( $\phi$ ) between two Rabi frequencies has been set to zero for simplification. Also, the phase difference between two dipoles (corresponding to emission channels  $|a_{1,2}\rangle \rightarrow |c\rangle$ ) is assumed to be  $\Delta\varphi = 0$ . In this section, we discuss the influence of the two phases on fluorescence spectra and QI factor.

First, we discuss the influence of the relative phase difference between Rabi frequencies on the linewidth of fluorescence spectra. Let us focus our discussion on the MO and EO resonance, as shown in Figs. 5(a) and 5(d). But the

analysis of other Mie resonances is similar. The quantum emitter is placed outside the sphere with a distance  $d = 100$  nm. For MO configuration [Fig. 5(a)], the QI factor is negative ( $F_x < F_y$ ). As a result, the central peak is broadened and the side peaks are narrowed when the relative phase between two Rabi frequencies is zero, as shown in Fig. 5(b) (blue dash-dot curve). When relative phase  $\phi = \pi/2$ , then the central peak becomes narrower while the side peaks turn broader [red dotted curve in Fig. 5(b)]. If we further increase the phase to  $\phi = \pi$ , then the central peak will further be narrowed into subnatural linewidth, while the side peaks will be broadened to much larger than natural linewidth [black solid curve in Fig. 5(b)]. As shown in Fig. 5(c), we can continuously vary the phase difference so that the spectral linewidth of sidebands or central peak can be successively controlled from subnatural narrowing or broadening to broadening or subnatural narrowing. In contrast, for the EO resonance [Fig. 5(d)], the QI factor is positive ( $F_x > F_y$ ). Compared with the MO resonance case, the same changes of phase difference will induce opposite varying tendencies to the spectral linewidths, as illustrated in Figs. 5(e) and 5(f). In both MO and EO cases, the summation of linewidths of triplet spectra is almost a constant, which is consistent with the dressed state prediction (with no phase difference) [33]. The modification of linewidth induced by the relative phase difference is a result of both QI and field-induced coherence [12]. In Ref. [12], the QI is

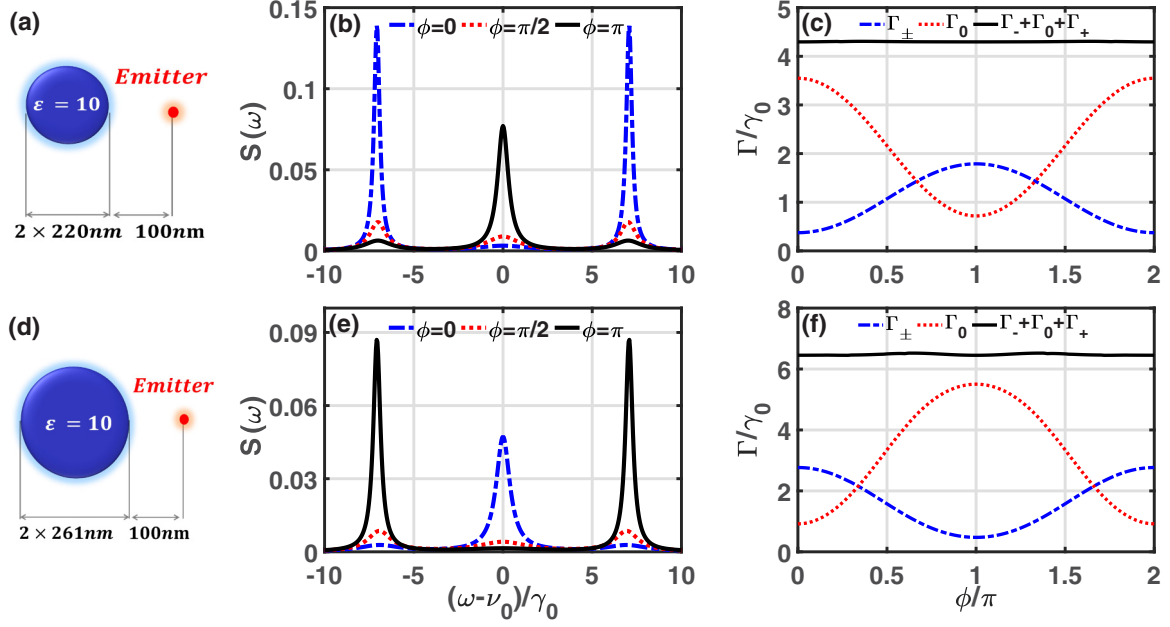


FIG. 5. The phase-induced additional modification of fluorescence spectra under Mie resonances. (a) The system setup for fluorescence control under magnetic octupole (MO) resonance. (b) The fluorescence spectra under MO resonance with relative phase difference  $\phi = 0, \pi/2, \pi$  (blue dash-dot, red dotted, and black solid curves, respectively). (c) The spectral linewidths for varying the relative phase under MO resonance; the blue (dash-dot) and red (dotted) curves correspond to the linewidths of the sideband and central peak. (d, e, f) The same as (a), (b), and (c), respectively, but the system is under electric octupole resonance. Here, the permittivity of the sphere is  $\epsilon = 10$  and the excitation wavelength is at  $\lambda_0 = 780$  nm; other parameters are  $\Omega = 5\gamma_0$ ,  $\omega_{12} = 0$ ,  $\Delta = 0$ ,  $\Delta\phi = 0$ .

provided by two parallel transition dipoles, while in this paper QI is supplied by Mie-resonances-induced AQV. Thus, with Mie-resonances-induced QI, a continuously varying phase difference can lead to continued linewidth modification from narrowing to broadening.

Next, we discuss the influence of dipole phase on QI factor. In the main text, we give the definition of effective QI factor in Eq. (3), which depends on dipole phase difference by a factor  $\cos(\Delta\phi)$ . Here, we give a numerical verification. With the same configurations as Figs. 5(a) and 5(d), we find the variation of  $\Delta\phi$  produces nearly the same spectral linewidth modification as that caused by relative phase difference between Rabi frequencies (Fig. 5). According to the dressed state analysis, the linewidth of the spectra reads  $\Gamma_0/\gamma_0 = (F_x + F_y)(1 - I_q)/2$  and  $\Gamma_{\pm}/\gamma_0 = (F_x + F_y)(1 + I_q)/4$  [33]. Then we have  $I_q = (\Gamma_0 - \Gamma_{\pm})/(\Gamma_0 + \Gamma_{\pm})$ , which helps to trace the QI factor from numerical calculated linewidth. Figure 6 shows the QI factors under MO (red and green concave curves) and EO (blue and black convex curves) resonances. We can see that the numerical results (solid curves) agree well with the analytical prediction (dashed curves).

Although both Rabi frequency phase ( $\phi$ ) and dipole phase ( $\Delta\phi$ ) can modulate the spectral linewidth similarly, their physics origins are different. The former is a coherent effect induced by laser field, while the latter is a result of AQV-induced QI. If both effects are taken into account, the total modification should be determined by a new factor  $I'_q = \text{Re}[\kappa \exp(i\phi)/\sqrt{\gamma_1\gamma_2}] = \cos(\Delta\phi + \phi)(F_x - F_y)/(F_x + F_y)$ . Therefore, the Mie resonances system we proposed has a large degree of freedom for emission spectral linewidth modification.

## VI. CONCLUSION

In this paper, we have investigated the anisotropy-induced QI effect and fluorescence narrowing of a four-level system under dielectric Mie resonances. We have shown that the QI effect can be nearly perfect due to the extreme AQV induced by Mie resonances. We have also demonstrated that the QI factor can be modified in a wide range by selecting different Mie resonances and the emitter's position. We have further found that the enhanced QI effect can dramatically modify the

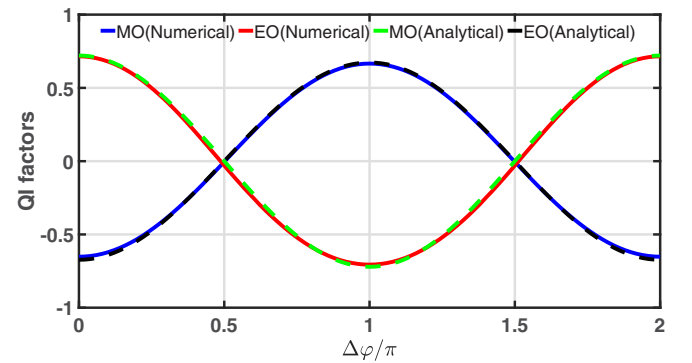


FIG. 6. QI factor modification caused by dipole phase under Mie resonances. The solid curves are results traced from numerical spectral linewidths, while the dashed curves are results predicted by analytical expression  $I_q = \cos(\Delta\phi)(F_x - F_y)/(F_x + F_y)$  (convex curves for MO mode, while concave curves for EO mode). All parameters are the same as in Fig. 5 except that the phase of Rabi frequency is zero.

spontaneous emission spectrum in the visible region, leading to subnatural narrowing of spectral linewidths. Our results also reveal that such QI-induced spectra narrowing effect is available in a larger area than in metallic nanoparticle systems. These results indicate that the high-index dielectric Mie resonant structure is a great platform to engineer nanoscale light-matter interaction, and our findings may have potential applications for integrated quantum photonics, such as high-performance quantum light sources on the chip.

#### ACKNOWLEDGMENTS

We thank Prof. J. Zhang for the helpful discussions. This work was supported by the National Natural Science Foundation of China (Grants No. 11974032, No. 11734001, and No. 11525414) and the Key Research and Development Program of Guangdong Province (Grant No. 2018B030329001).

#### APPENDIX A: THE SCATTERING CROSS SECTION OF A DIELECTRIC SPHERE

Considering a plane wave illuminates the dielectric sphere in Fig. 1, the electromagnetic wave will be scattered by the sphere. The scattering cross section is defined as [59]  $\sigma_{\text{sca}} = W_{\text{sca}}/I_{\text{in}}$ , where  $W_{\text{sca}}$  is scattered field power and  $I_{\text{in}}$  is the intensity of the incident plane wave. Performing the Mie expansion to the electromagnetic field and applying the boundary conditions, then one can work out  $\sigma_{\text{sca}}$  [59]:

$$\sigma_{\text{sca}} = \frac{2\pi}{k_0^2} \sum_{n=1}^{+\infty} (2n+1) (|a_n|^2 + |b_n|^2), \quad (\text{A1})$$

where  $k_0$  is the incident wave number in air, and  $a_n$  and  $b_n$  are electric and magnetic Mie coefficients that read

$$a_n = \frac{m\psi_n(mX)\psi'_n(X) - \psi_n(X)\psi'_n(mX)}{m\psi_n(mX)\xi'_n(X) - \xi_n(X)\psi'_n(mX)}, \quad (\text{A2a})$$

$$b_n = \frac{\psi_n(mX)\psi'_n(X) - m\psi_n(X)\psi'_n(mX)}{\psi_n(mX)\xi'_n(X) - m\xi_n(X)\psi'_n(mX)}, \quad (\text{A2b})$$

with  $X = k_0R$ ,  $m = \sqrt{\varepsilon}$ . Here,  $\psi_n(x) = xj_n(x)$  and  $\xi_n(x) = xh_n^{(1)}(x)$  are so-called Riccati-Bessel functions,  $j_n(x)$  is the spherical Bessel function,  $h_n^{(1)}(x)$  is the spherical Hankel function of the first kind,  $\psi'_n(x) = d\psi_n(x)/dx$ , and  $\xi'_n(x) = d\xi_n(x)/dx$ .

In our numerical calculation, we mainly focus on the first six lowest Mie resonant modes, and the infinite series in Eq. (A1) is truncated at 20 terms, which is enough to ensure the accuracy of our results.

#### APPENDIX B: THE PURCELL FACTOR FOR A DIELECTRIC SPHERE

The Purcell factor can be obtained classically using the fact the emission rate of a quantum dipole is in proportion to its radiated power. So we can calculate the Purcell factor by  $F_\theta = \gamma(\theta)/\gamma_0 = W_\theta/W_0$ , where  $W_0$  is the radiated power of a classical dipole buried in an infinite homogeneous vacuum and  $W_\theta$  is the radiated power of a classical dipole placed near the dielectric sphere we investigated, with the dipole orientation angle  $\theta$ . Following this method, the expressions

of the Purcell factor have been given in Ref. [63], for a dipole outside the dielectric sphere:

$$F_x = \frac{3}{2} \sum_{n=1}^{+\infty} n(n+1)(2n+1) \times \left| \frac{j_n(Y_1) - a_n h_n^{(1)}(Y_1)}{Y_1} \right|^2, \quad (\text{B1a})$$

$$F_y = \frac{3}{4} \sum_{n=1}^{+\infty} (2n+1) \left\{ \left| j_n(Y_1) - b_n h_n^{(1)}(Y_1) \right|^2 + \left| \frac{\psi'_n(Y_1) - a_n \xi'_n(Y_1)}{Y_1} \right|^2 \right\}, \quad (\text{B1b})$$

with  $Y_1 = k_0(R+d)$ . For a dipole inside the dielectric sphere, we have [63]

$$F_x = \frac{3m^2}{2X^2} \sum_{n=1}^{+\infty} n(n+1)(2n+1) \left| \frac{j_n(mY_2)}{mY_2 E_n} \right|^2, \quad (\text{B2a})$$

$$F_y = \frac{3m^2}{4X^2} \sum_{n=1}^{+\infty} (2n+1) \times \left( \left| \frac{\psi'_n(mY_2)}{mY_2 E_n} \right|^2 + \left| \frac{j_n(mY_2)}{mM_n} \right|^2 \right), \quad (\text{B2b})$$

with  $Y_2 = k_0(R-d)$ ,  $E_n = m^2 j_n(mX)\xi'_n(X) - h_n^{(1)}(X)\psi'_n(mX)$ ,  $M_n = j_n(mX)\xi'_n(X) - h_n^{(1)}(X)\psi'_n(mX)$ . Also, the infinite series in Eqs. (B1) and (B2) are truncated at 20 terms in our numerical calculation.

#### APPENDIX C: THE QI ENHANCEMENT EFFECT WITH DETUNING

In this section, we give a more detailed explanation for the off-resonant QI enhancement effect discussed in Sec. III A. Here, we take the detuned ED mode structure with a radius  $R = 138$  nm as an example [corresponding to the local maximum of QI factor near the ED mode in Fig. 2(b)]. The discussion for higher-order electric resonances is similar.

First, let us consider the spectral feature of electric-type resonance. Figure 7(a) shows the scattering cross section contributed by ED and MD (proportional to modular square of Mie coefficients  $|a_1|^2$  and  $|b_1|^2$ ). For radius  $R = 138$  nm, we can see that the central resonant wavelength for ED and MD is 713 and 915 nm. It is obvious that the linewidth of the ED mode is very large and the linewidth is much broader than the one of the MD mode. Although ED and MD spectral curves are overlapping, the ED resonances dominate the excitation when the wavelength detunes from the ED resonance center to 780 nm.

Then, we consider the AQV modification when the wavelength detunes from ED resonance. As shown in Fig. 7(b), the Purcell factor for the  $x$ -polarized dipole ( $F_x$ , blue solid curve) keeps at a higher level than the  $y$ -polarized one ( $F_y$ , red dotted curve) under exact ED resonance (at central wavelength), resulting in a high AQV. With detuning to  $\lambda_0 = 780$  nm, the Purcell enhancement of  $F_x$  still dominates due to broadband ED resonance, while  $F_y$  is largely suppressed because of weak

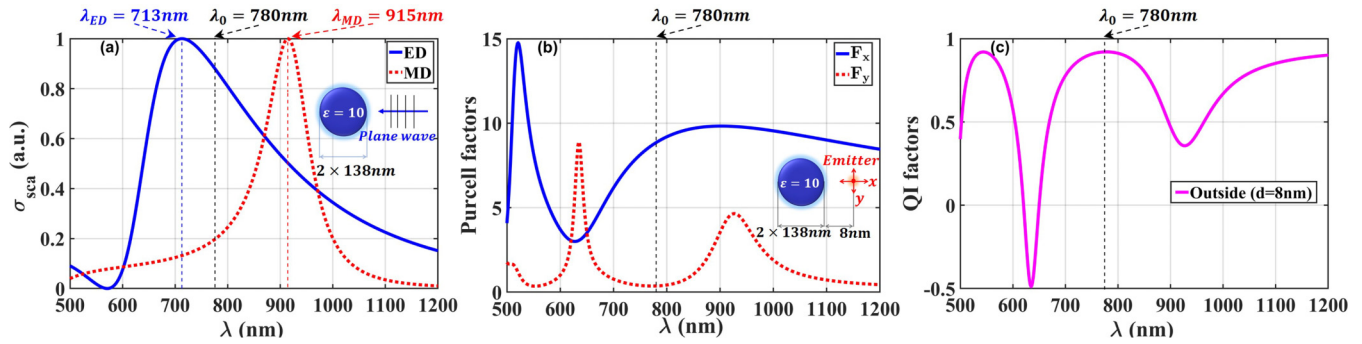


FIG. 7. The QI enhancement effect in resonance-detuned structure. (a) Scattering cross section  $\sigma_{sca}$  decomposition of ED (blue solid curve) and MD (red dotted curve) modes as a function of excitation wavelength  $\lambda$  for an incident plane wave. (b) Anisotropic Purcell factors as a function of excitation wavelength  $\lambda$  for an emitter outside the sphere. The blue (solid) and red (dotted) curves correspond to  $x$ - and  $y$ -polarized transition dipole moments. (c) QI factor for varying wavelength  $\lambda$ . Here, the sphere's radius is  $R = 138$  nm, the permittivity of the sphere is  $\epsilon = 10$ , and the distance between the emitter and sphere is  $d = 8$  nm.

MD excitation. So, the AQV is strengthened with this small detuning. If the detuning keeps increasing,  $F_y$  will increase owing to dominant MD resonance, i.e., the AQV becomes weaker for the larger detuning. As a result, the strongest AQV arises near the off-resonant wavelength  $\lambda_0 = 780$  nm.

Consequently, with  $R = 138$  nm, the largest QI factor within the ED resonant band is obtained under a small detuning condition rather than the exact resonant condition (in the resonant center), as illustrated in Fig. 7(c). Note that such a detuning QI enhancement effect happens in the electric-type

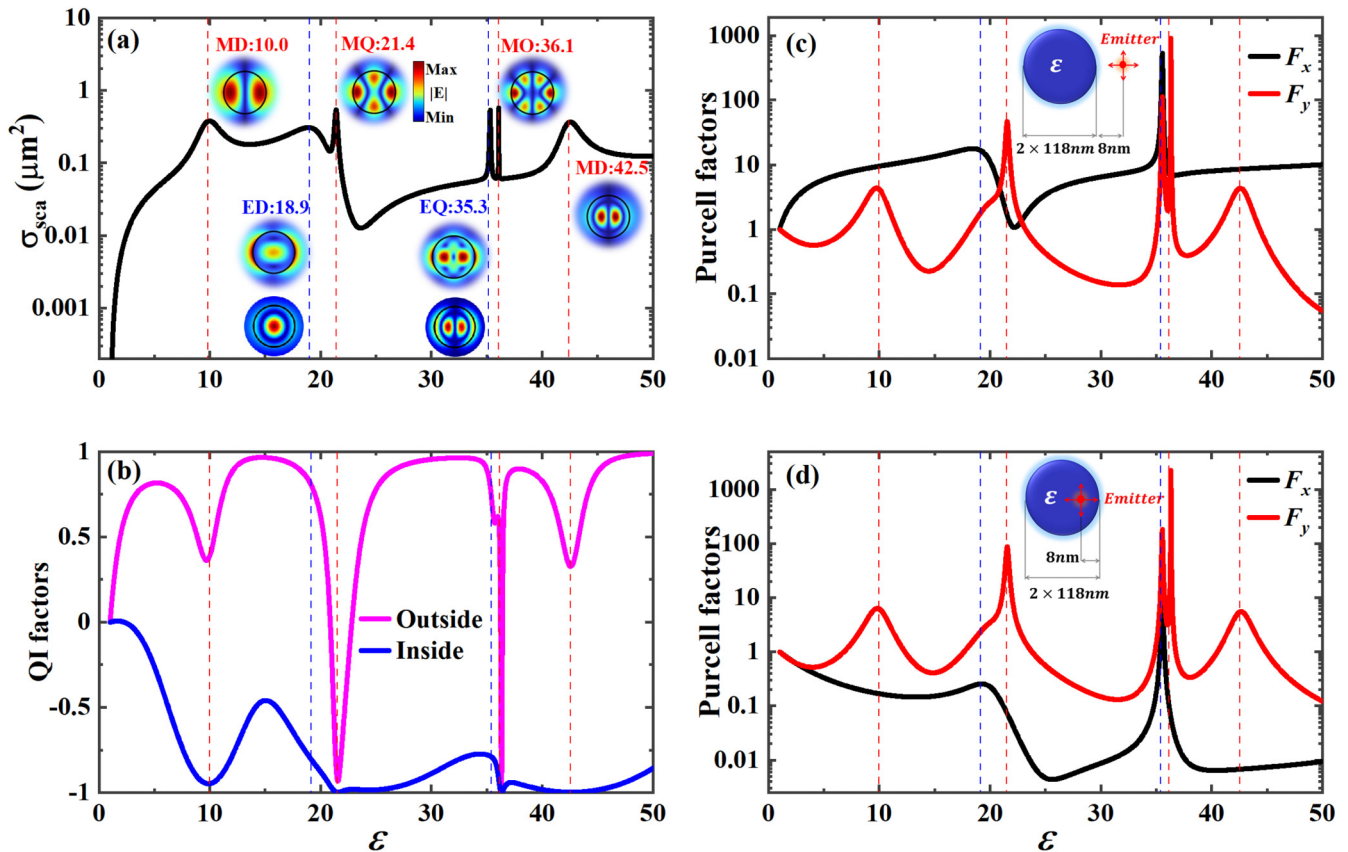


FIG. 8. Enhanced QI effect with varying sphere permittivity  $\epsilon$ . (a) Scattering cross section  $\sigma_{sca}$  as a function of permittivity  $\epsilon$  for an incident plane wave. The insets show the near-field patterns of the first five Mie resonances (the sixth mode is magnetic dipole resonance, similar to the first one); the dashed lines and the texts indicate  $\epsilon$  for each resonance. (b) QI factor for varying permittivity  $\epsilon$ . The pink (upper) curve denotes the quantum emitter outside the sphere, and the blue (lower) curve denotes the emitter inside the sphere. Anisotropic Purcell factors of an emitter (c) outside and (d) inside the sphere are presented. The black (two-peaked) and red (five-peaked) curves correspond to  $x$ - and  $y$ -polarized transition dipole moments. Insets in (c) and (d) illustrate the system setup for dipole outside and inside cases. In all figures, the sphere's radius is  $R = 118$  nm and the excitation wavelength is at  $\lambda_0 = 780$  nm.

resonant band, and thus it relies on the existence of electric resonances.

#### APPENDIX D: THE INFLUENCE OF PERMITTIVITY $\epsilon$ ON QI

In this section, the QI enhancement is further verified when Mie resonances are excited under different sphere permittivities  $\epsilon$ . We start from Mie resonances of the dielectric sphere with different permittivities. Figure 8(a) presents the scattering cross-section  $\sigma_{\text{sca}}$  variation as  $\epsilon$  changes. Here, the sphere's radius is  $R = 118$  nm and the excitation wavelength is at  $\lambda_0 = 780$  nm. As permittivity  $\epsilon$  increases from 1 to 50, six resonant peaks appear sequentially, corresponding to MD (1), ED, MQ, EQ, MO, and MD (2) resonances [59], respectively. The dashed lines and texts in Fig. 8(a) mark the resonant permittivity, while the insets show the corresponding near-field distributions. Here, the sixth peak is the MD resonance with a higher permittivity, where a larger portion of the fields is localized inside the sphere compared to the first resonance. We can observe that the higher-order Mie resonances (MQ, MO, and EQ) are more sensitive to the changes of  $\epsilon$ , while dipole resonances (ED and MD) are relatively insensitive to the changes of  $\epsilon$ . The near-field distributions are similar to those in Fig. 2(a), but the higher permittivity leads to much tighter field confinement. These changes in near-field distributions will lead to a more extreme AQV environment.

Then, we consider anisotropic Purcell factors and AQVs induced by tightly confined Mie resonances. Figures 8(c) and 8(d) show the variation of Purcell factors as  $\epsilon$  changes when the emitter is outside and inside the sphere, respectively. It is similar to the former results that  $x$ - and  $y$ -polarized emitters can efficiently excite the electric- and magnetic-type resonances, with the same physical origin as discussed in Sec. III A. But Purcell factors increase by one to two orders of magnitude compared to those in Fig. 2, which is caused by the stronger near-field enhancement under higher permittivity conditions [44]. Thanks to the significant improvement of anisotropy of the near field, a more extreme AQV environment is created. In addition, a high AQV is also obtained in some off-resonant regions, such as between MQ and EQ modes. For the emitter outside the sphere, such a large AQV arises from weak Purcell enhancement of  $F_x$  and suppression of  $F_y$  in the off-resonant region, which is similar to the result reported in some literature [23,25–27,32,37,41]. In contrast, for the emitter inside the sphere, the high AQV results from the difference in the suppressive degrees between Purcell factors  $F_x$  and  $F_y$ . Thus, the existence of anisotropic Purcell enhancement and suppression leads to a large AQV in the higher-permittivity structure.

Next, the QI enhancement induced by AQV under these tightly confined Mie resonances is investigated. Figure 8(b) illustrates the variation of QI factors as a function of  $\epsilon$ . The pink (upper) and blue (lower) curves show the results when the emitter is outside and inside the sphere. The magnitudes of QI factors are greater than 0.5 (except for MD resonance with  $I_q \approx 0.35$ ) when  $\epsilon$  fulfills the on-resonant condition (dashed lines), which is a result of large AQV under Mie resonances. We can even obtain nearly perfect quantum interference with

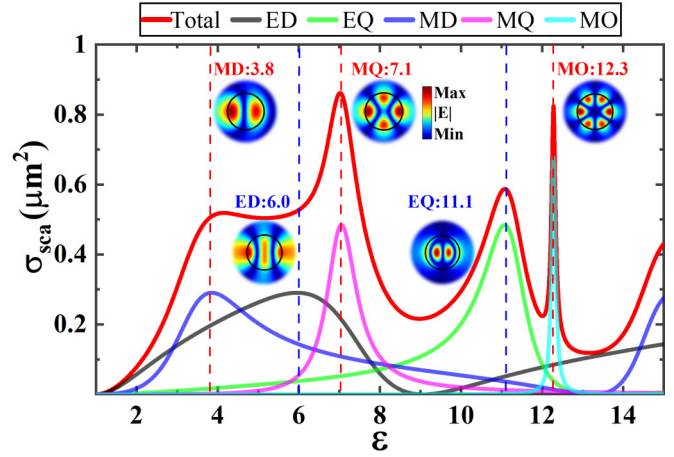


FIG. 9. Mie resonances in a larger sphere with smaller permittivity. The black curve is scattering cross section  $\sigma_{\text{sca}}$  as a function of permittivity  $\epsilon$  for an incident plane wave. The insets show the near-field patterns of the first five Mie resonances; the dashed lines and the texts indicate  $\epsilon$  for each resonance. The other colored curves are multipole decomposition of the  $\sigma_{\text{sca}}$  for the first five Mie resonances. Here, the sphere's radius is  $R = 200$  nm and the excitation wavelength is at  $\lambda_0 = 780$  nm.

$I_q \approx -1$  as magnetic resonances appear. What is more, a very large QI factor can be obtained over a broad parameter region due to off-resonant induced AQV. As seen in Fig. 8(b), the QI factor curve is nearly flat with  $I_q > 0.9$  when the system is near the EQ mode (purple curve) or the second MD mode [blue (lower) curve]. Hence, producing a strong QI enhancement is easier via a higher-permittivity sphere.

Moreover, we discuss the sign modulation of the QI factor by these tightly confined Mie resonances. As shown in Fig. 8(b), for the emitter outside the sphere [purple (upper) curve], the QI factor ranges from a positive to negative value when the Mie resonance transitions from the electric type to magnetic type. The QI factor changes sharply from  $-1$  to  $+1$ , owing to the sensitive response of Mie resonances to  $\epsilon$ . We have discussed in Sec. III A that the sign modulation comes from the polarization-dependent Purcell enhancement. Thus, Mie resonances with high permittivity can provide a sharp and full-range modulation to the QI factor. In the above discussion, we showed that a high permittivity of the sphere ensures the existence of Mie resonances with a very small radius  $R = 118$  nm. While a realistic dielectric material in the visible region may have a high permittivity up to approximately 10, as reviewed in Ref. [66], it is not as large as discussed in the above context. Nonetheless, the above discussion remains valid for a sphere with a relatively larger radius. Figure 9 shows the scattering cross section  $\sigma_{\text{sca}}$  for a sphere with  $R = 200$  nm; we can see that the first five Mie resonances can be obtained when permittivity  $\epsilon$  varies from 1 to 15. So the modulation to QI is also available in such a structure. We notice that sharp and large modulation of QI were also obtained in the literature [22,25], where a negative-refractive-index phase compensator is used in photonic crystals or Fabry-Pérot cavity structures. To obtain such a large QI modulation in the visible region, the method described in

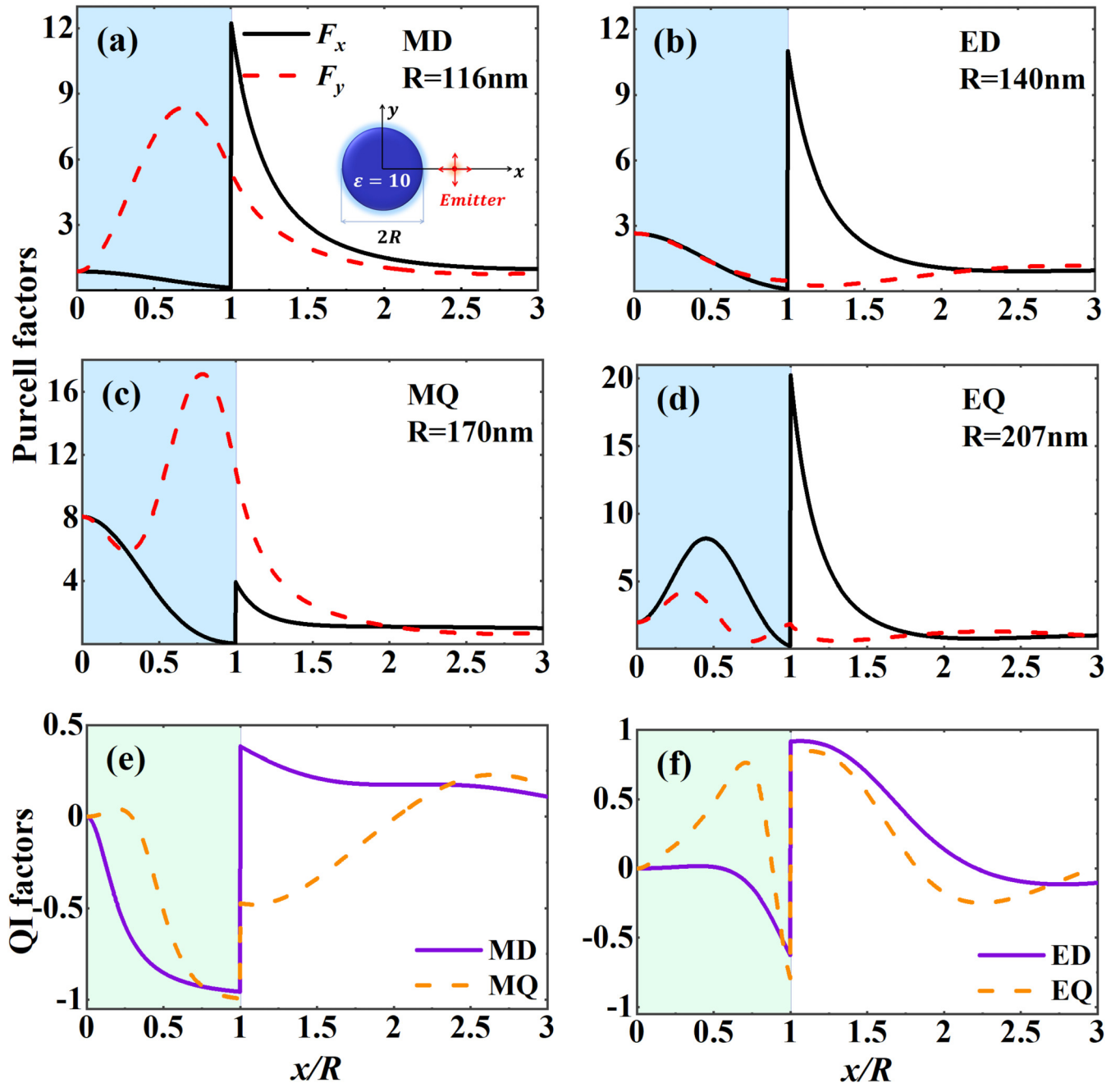


FIG. 10. Position-dependent quantum interference. Purcell factors as a function of  $x/R$  for (a) magnetic dipole, (b) electric dipole, (c) magnetic quadrupole, and (d) electric quadrupole resonances. The black (solid) and red (dashed) curves correspond to  $x$ - and  $y$ -polarized transition dipole moments. The inset in (a) shows the system setup with the emitter's position variation. The variations of corresponding QI factors are demonstrated in (e) for magnetic resonances and (f) for electric resonances. The position of the quantum emitter is normalized to resonant radius  $R$ , and the regions filled with pale blue and green represent the position inside the sphere. Here, the permittivity of the sphere is  $\epsilon = 10$  and the excitation wavelength is at  $\lambda_0 = 780$  nm.

Refs. [22,25] faces the challenge of reducing absorption in negative index materials, while our scheme demands precise control of the geometry size of the Mie resonator.

#### APPENDIX E: THE INFLUENCE OF EMITTER POSITION ON QI

We further explore the modulation of QI enhancement induced by the local field of Mie resonances. To this end,

we first consider the anisotropic Purcell factors and AQV features with different emitter positions for a given resonance. Figures 10(a)–10(d) show the Purcell factors as a function of emitter position  $x$  for the first four Mie resonances MD ( $R = 116$  nm), ED ( $R = 140$  nm), MQ ( $R = 170$  nm), and EQ ( $R = 207$  nm), respectively. Here, the sphere's permittivity is  $\epsilon = 10$  and the excitation wavelength is at  $\lambda_0 = 780$  nm. For simplification, the emitter's position is normalized to the corresponding resonant radius and the region inside the

sphere ( $x/R < 1$ ) is filled with pale blue. We can see that for magnetic resonances in Figs. 10(a) and 10(c) [for electric resonances in Figs. 10(b) and 10(d)], the Purcell factor  $F_y$  ( $F_x$ ) has a profile similar to the corresponding resonant near-field distribution. This is because the position with a stronger local field intensity has a larger Purcell enhancement. Simultaneously, the  $x$ - or  $y$ -polarized emitter can excite electric or magnetic resonances more efficiently, which leads to an AQV. For these four resonances, a large AQV arises near the sphere's surface. In addition, a relatively large AQV also appears in the position of  $x/R \approx 0.5$  for the EQ resonance because of the large difference between  $F_x$  and  $F_y$ . It is obvious that the Purcell factor is isotropic at the sphere center due to geometry symmetry, and then the AQV vanishes. Hence, the variation of the emitter's position can lead to a large modulation of AQV, which will directly influence the QI.

Then, the QI enhancement with different emitter positions is considered. Figures 10(e) and 10(f) illustrate the variation of QI factors as a function of  $x$  for magnetic and electric resonances, respectively. Here, the region inside the sphere ( $x/R < 1$ ) is filled with pale green. When the emitter is located at the center of the sphere ( $x = 0$ ), there is no QI effect ( $I_q = 0$ ). As the emitter moves toward the sphere's surface ( $0 < x/R < 1$ ), the QI factor almost continuously decreases from 0 to  $-1$  for MD, MQ, and ED resonances, while for the EQ resonance the QI factor first increases to 0.8, then decreases to  $-0.8$  approximately as the emitter approaches the sphere's surface. Such modulation of the QI factor comes

from the large AQV in the hot spots. As the emitter keeps away from the sphere's surface ( $x/R > 1$ ), the QI factor gradually decays to zero and QI vanishes, just like the behaviors of the QI in many other nanostructures [21,23,26,32,37,39,41]. But the large QI factor regions with  $|I_q| > 0.5$  can still cover a wide range of  $\Delta x \sim R$ . Within the region, a spatial range of 100 nm can contribute to a Purcell factor smaller than 1. This area can lead to an effective narrowing of the spectral linewidth, which is several times broader than that in plasmonic structures [33–35]. Hence, the QI factor can be modified in a wide range by selecting the emitter's position, and a large QI factor is available in a relatively broad spatial region.

Furthermore, we discuss the modulation to the sign of the QI factor with different emitter positions. First, the sign can be changed when the emitter moves across the sphere's surface. As shown in Figs. 10(e) and 10(f), the QI factor is negative on the inner surface and becomes positive on the outer surface for MD, ED, and MQ resonances. The sudden change of the QI factor's sign comes from the discontinuous anisotropic near field. Second, the sign can be changed when the emitter moves from one hot spot to another hot spot in the high-order resonant structure. For example, in the MQ resonant structure [Fig. 10(f)], the QI factor is positive ( $I_q \approx +0.8$ ) at the position  $x/R \approx 0.5$ , while it becomes negative ( $I_q \approx -0.8$ ) at the position  $x/R \approx 1$ . Therefore, the movement of the emitter's position provides a convenient way to modulate the sign of the QI factor.

- 
- [1] J. Javanainen, Effect of state superpositions created by spontaneous emission on laser-driven transitions, *Europhys. Lett.* **17**, 407 (1992).
- [2] M. O. Scully, S.-Y. Zhu, and A. Gavrielides, Degenerate Quantum-Beat Laser: Lasing without Inversion and Inversion without Lasing, *Phys. Rev. Lett.* **62**, 2813 (1989).
- [3] S. E. Harris, Lasers without Inversion: Interference of Lifetime-Broadened Resonances, *Phys. Rev. Lett.* **62**, 1033 (1989).
- [4] M. Fleischhauer, C. H. Keitel, L. M. Narducci, M. O. Scully, S.-Y. Zhu, and M. Zubairy, Lasing without inversion: interference of radiatively broadened resonances in dressed atomic systems, *Opt. Commun.* **94**, 599 (1992).
- [5] S. Menon and G. S. Agarwal, Effects of spontaneously generated coherence on the pump-probe response of a  $\Lambda$  system, *Phys. Rev. A* **57**, 4014 (1998).
- [6] E. Paspalakis, N. J. Kylstra, and P. L. Knight, Transparency Induced via Decay Interference, *Phys. Rev. Lett.* **82**, 2079 (1999).
- [7] S.-Y. Zhu and M. O. Scully, Spectral Line Elimination and Spontaneous Emission Cancellation via Quantum Interference, *Phys. Rev. Lett.* **76**, 388 (1996).
- [8] P. Zhou and S. Swain, Quantum interference in resonance fluorescence for a driven  $v$  atom, *Phys. Rev. A* **56**, 3011 (1997).
- [9] H. Lee, P. Polynkin, M. O. Scully, and S.-Y. Zhu, Quenching of spontaneous emission via quantum interference, *Phys. Rev. A* **55**, 4454 (1997).
- [10] Z. Ficek and T. Rudolph, Quantum interference in a driven two-level atom, *Phys. Rev. A* **60**, R4245(R) (1999).
- [11] Y. He, Y.-M. He, J. Liu, Y.-J. Wei, H. Y. Ramírez, M. Atatüre, C. Schneider, M. Kamp, S. Höfling, C.-Y. Lu, and J.-W. Pan, Dynamically Controlled Resonance Fluorescence Spectra from a Doubly Dressed Single InGaAs Quantum Dot, *Phys. Rev. Lett.* **114**, 097402 (2015).
- [12] E. Paspalakis and P. L. Knight, Phase Control of Spontaneous Emission, *Phys. Rev. Lett.* **81**, 293 (1998).
- [13] C. H. Keitel, Narrowing Spontaneous Emission without Intensity Reduction, *Phys. Rev. Lett.* **83**, 1307 (1999).
- [14] Y. Niu and S. Gong, Enhancing Kerr nonlinearity via spontaneously generated coherence, *Phys. Rev. A* **73**, 053811 (2006).
- [15] Z.-H. Tang, G.-X. Li, and Z. Ficek, Entanglement created by spontaneously generated coherence, *Phys. Rev. A* **82**, 063837 (2010).
- [16] Z.-H. Tang and G.-X. Li, Entanglement of a two-mode field in a collective three-level atomic system, *Phys. Rev. A* **84**, 063801 (2011).
- [17] G. S. Agarwal, Anisotropic Vacuum-Induced Interference in Decay Channels, *Phys. Rev. Lett.* **84**, 5500 (2000).
- [18] M. Pelton, Modified spontaneous emission in nanophotonic structures, *Nat. Photonics* **9**, 427 (2015).
- [19] Z. Qian, L. Shan, X. Zhang, Q. Liu, Y. Ma, Q. Gong, and Y. Gu, Spontaneous emission in micro-or nanophotonic structures, *PhotonIX* **2**, 21 (2021).
- [20] W. L. Vos, A. F. Koenderink, and I. S. Nikolaev, Orientation-dependent spontaneous emission rates of a two-level quantum

- emitter in any nanophotonic environment, *Phys. Rev. A* **80**, 053802 (2009).
- [21] G.-X. Li, F.-L. Li, and S.-Y. Zhu, Quantum interference between decay channels of a three-level atom in a multilayer dielectric medium, *Phys. Rev. A* **64**, 013819 (2001).
- [22] J.-P. Xu, L.-G. Wang, Y.-P. Yang, Q. Lin, and S.-Y. Zhu, Quantum interference between two orthogonal transitions of an atom in one-dimensional photonic crystals, *Opt. Lett.* **33**, 2005 (2008).
- [23] Y. Yang, J. Xu, H. Chen, and S. Zhu, Quantum Interference Enhancement with Left-Handed Materials, *Phys. Rev. Lett.* **100**, 043601 (2008).
- [24] J.-P. Xu, Y.-P. Yang, Q. Lin, and S.-Y. Zhu, Spontaneous decay of a two-level atom near the left-handed slab, *Phys. Rev. A* **79**, 043812 (2009).
- [25] J.-P. Xu and Y.-P. Yang, Quantum interference of v-type three-level atom in structures made of left-handed materials and mirrors, *Phys. Rev. A* **81**, 013816 (2010).
- [26] X. Zeng, J. Xu, and Y. Yang, Spontaneous emission interference enhancement with a  $\mu$ -negative metamaterial slab, *Phys. Rev. A* **84**, 033834 (2011).
- [27] L. Sun and C. Jiang, Quantum interference in a single anisotropic quantum dot near hyperbolic metamaterials, *Opt. Express* **24**, 7719 (2016).
- [28] P. K. Jha, X. Ni, C. Wu, Y. Wang, and X. Zhang, Metasurface-Enabled Remote Quantum Interference, *Phys. Rev. Lett.* **115**, 025501 (2015).
- [29] P. K. Jha, N. Shitrit, X. Ren, Y. Wang, and X. Zhang, Spontaneous Exciton Valley Coherence in Transition Metal Dichalcogenide Monolayers Interfaced with an Anisotropic Metasurface, *Phys. Rev. Lett.* **121**, 116102 (2018).
- [30] M. Sohoni, P. K. Jha, M. Nalabothula, and A. Kumar, Interlayer exciton valleytronics in bilayer heterostructures interfaced with a phase gradient metasurface, *Appl. Phys. Lett.* **117**, 121101 (2020).
- [31] E. Lassalle, P. Lalanne, S. Aljunid, P. Genevet, B. Stout, T. Durt, and D. Wilkowski, Long-lifetime coherence in a quantum emitter induced by a metasurface, *Phys. Rev. A* **101**, 013837 (2020).
- [32] V. Yannopapas, E. Paspalakis, and N. V. Vitanov, Plasmon-Induced Enhancement of Quantum Interference near Metallic Nanostructures, *Phys. Rev. Lett.* **103**, 063602 (2009).
- [33] Y. Gu, L. Wang, P. Ren, J. Zhang, T. Zhang, O. J. Martin, and Q. Gong, Surface-plasmon-induced modification on the spontaneous emission spectrum via subwavelength-confined anisotropic Purcell factor, *Nano Lett.* **12**, 2488 (2012).
- [34] F. Carreño, M. A. Antón, V. Yannopapas, and E. Paspalakis, Resonance fluorescence spectrum of a  $\Lambda$ -type quantum emitter close to a metallic nanoparticle, *Phys. Rev. A* **94**, 013834 (2016).
- [35] F. Carreño, M. A. Antón, V. Yannopapas, and E. Paspalakis, Control of resonance fluorescence of a four-level quantum emitter near a plasmonic nanostructure, *Phys. Rev. A* **95**, 043825 (2017).
- [36] H. Chen, J. Ren, Y. Gu, D. Zhao, J. Zhang, and Q. Gong, Nanoscale Kerr nonlinearity enhancement using spontaneously generated coherence in plasmonic nanocavity, *Sci. Rep.* **5**, 18315 (2016).
- [37] D. Karaoulanis, E. Paspalakis, and V. Yannopapas, Quantum interference near bismuth-chalcogenide microstructures, *J. Opt. Soc. Am. B* **38**, 3301 (2021).
- [38] V. Karanikolas and E. Paspalakis, Plasmon-induced quantum interference near carbon nanostructures, *J. Phys. Chem. C* **122**, 14788 (2018).
- [39] X. Zeng, Z. Li, G.-Q. Ge, and M. S. Zubairy, Quantum interference near graphene layers: observing the surface plasmons with transverse electric polarization, *Phys. Rev. A* **99**, 043811 (2019).
- [40] I. Thanopoulos, V. Karanikolas, and E. Paspalakis, Non-Markovian spontaneous emission interference near a MoS<sub>2</sub> nanodisk, *Opt. Lett.* **44**, 3510 (2019).
- [41] R. Zeng, M. Zhang, C. Wang, X. Qian, H. Li, Q. Li, Y. Yang, and S. Zhu, Spontaneous emission interference in topological insulator multilayers, *J. Opt. Soc. Am. B* **36**, 1890 (2019).
- [42] S. Hughes and G. S. Agarwal, Anisotropy-Induced Quantum Interference and Population Trapping between Orthogonal Quantum Dot Exciton States in Semiconductor Cavity Systems, *Phys. Rev. Lett.* **118**, 063601 (2017).
- [43] A. I. Kuznetsov, A. E. Miroschnichenko, M. L. Brongersma, Y. S. Kivshar, and B. Luk'yanchuk, Optically resonant dielectric nanostructures, *Science* **354**, aag2472 (2016).
- [44] K. Koshelev and Y. Kivshar, Dielectric resonant metaphotonics, *ACS Photonics* **8**, 102 (2020).
- [45] A. B. Evlyukhin, S. M. Novikov, U. Zywietz, R. L. Eriksen, C. Reinhardt, S. I. Bozhevolnyi, and B. N. Chichkov, Demonstration of magnetic dipole resonances of dielectric nanospheres in the visible region, *Nano Lett.* **12**, 3749 (2012).
- [46] Y. Zhao, Y. Yang, and H.-B. Sun, Nonlinear meta-optics towards applications, *Photonix* **2**, 3 (2021).
- [47] T. Shi, Z.-L. Deng, Q.-A. Tu, Y. Cao, and X. Li, Displacement-mediated bound states in the continuum in all-dielectric superlattice metasurfaces, *Photonix* **2**, 7 (2021).
- [48] W. Liu, Generalized Magnetic Mirrors, *Phys. Rev. Lett.* **119**, 123902 (2017).
- [49] M. V. Rybin, K. L. Koshelev, Z. F. Sadrieva, K. B. Samusev, A. A. Bogdanov, M. F. Limonov, and Y. S. Kivshar, High- $Q$  Supercavity Modes in Subwavelength Dielectric Resonators, *Phys. Rev. Lett.* **119**, 243901 (2017).
- [50] K. Koshelev, S. Kruk, E. Melik-Gaykazyan, J.-H. Choi, A. Bogdanov, H.-G. Park, and Y. Kivshar, Subwavelength dielectric resonators for nonlinear nanophotonics, *Science* **367**, 288 (2020).
- [51] T. Feng, Y. Xu, W. Zhang, and A. E. Miroschnichenko, Ideal Magnetic Dipole Scattering, *Phys. Rev. Lett.* **118**, 173901 (2017).
- [52] A. Bag, M. Neugebauer, P. Woźniak, G. Leuchs, and P. Banzer, Transverse Kerker Scattering for Angstrom Localization of Nanoparticles, *Phys. Rev. Lett.* **121**, 193902 (2018).
- [53] H. K. Shamkhi, K. V. Baryshnikova, A. Sayanskiy, P. Kapitanova, P. D. Terekhov, P. Belov, A. Karabchevsky, A. B. Evlyukhin, Y. Kivshar, and A. S. Shalin, Transverse Scattering and Generalized Kerker Effects in All-Dielectric Mie-Resonant Metaoptics, *Phys. Rev. Lett.* **122**, 193905 (2019).
- [54] F. Qin, Z. Zhang, K. Zheng, Y. Xu, S. Fu, Y. Wang, and Y. Qin, Transverse Kerker Effect for Dipole Sources, *Phys. Rev. Lett.* **128**, 193901 (2022).
- [55] J. R. Zurita-Sánchez, Anapole arising from a mie scatterer with dipole excitation, *Phys. Rev. Res.* **1**, 033064 (2019).

- [56] J. R. Zurita-Sánchez, Anapole due to a tangentially polarized dipole near a subwavelength sphere: Inhibition and enhancement of spontaneous emission, *Phys. Rev. A* **104**, 053524 (2021).
- [57] J. W. Choong, N. Nefedkin, and A. Krasnok, Collectively driven optical nanoantennas, *Phys. Rev. A* **103**, 043714 (2021).
- [58] E. Zanganeh, A. Evlyukhin, A. Miroshnichenko, M. Song, E. Nenasheva, and P. Kapitanova, Anapole Meta-Atoms: Nonradiating Electric and Magnetic Sources, *Phys. Rev. Lett.* **127**, 096804 (2021).
- [59] C. F. Bohren and D. R. Huffman, *Absorption and Scattering of Light by Small Particles* (Wiley, New York, 2008).
- [60] L. Onsager, Electric moments of molecules in liquids, *J. Am. Chem. Soc.* **58**, 1486 (1936).
- [61] H. T. Dung, S. Y. Buhmann, and D.-G. Welsch, Local-field correction to the spontaneous decay rate of atoms embedded in bodies of finite size, *Phys. Rev. A* **74**, 023803 (2006).
- [62] H. J. Carmichael, *Statistical Methods in Quantum Optics I: Master Equations and Fokker-Planck Equations* (Springer, New York, 1999), Vol. 1.
- [63] H. Chew, Transition rates of atoms near spherical surfaces, *J. Chem. Phys.* **87**, 1355 (1987).
- [64] J. R. Johansson, P. D. Nation, and F. Nori, Qutip: An open-source python framework for the dynamics of open quantum systems, *Comput. Phys. Commun.* **183**, 1760 (2012).
- [65] K. J. Russell, T.-L. Liu, S. Cui, and E. L. Hu, Large spontaneous emission enhancement in plasmonic nanocavities, *Nat. Photonics* **6**, 459 (2012).
- [66] D. G. Baranov, D. A. Zuev, S. I. Lepeshov, O. V. Kotov, A. E. Krasnok, A. B. Evlyukhin, and B. N. Chichkov, All-dielectric nanophotonics: The quest for better materials and fabrication techniques, *Optica* **4**, 814 (2017).
- [67] H. Schniepp and V. Sandoghdar, Spontaneous Emission of Europium Ions Embedded in Dielectric Nanospheres, *Phys. Rev. Lett.* **89**, 257403 (2002).
- [68] C. Bradac, W. Gao, J. Forneris, M. E. Trusheim, and I. Aharonovich, Quantum nanophotonics with group iv defects in diamond, *Nat. Commun.* **10**, 5625 (2019).
- [69] P. Lodahl, S. Mahmoodian, and S. Stobbe, Interfacing single photons and single quantum dots with photonic nanostructures, *Rev. Mod. Phys.* **87**, 347 (2015).